

RICE UNIVERSITY

Low frequency plasma waves at Mars

by

Jared R. Espley

A THESIS SUBMITTED
IN PARTIAL FULFILLMENT OF THE
REQUIREMENTS FOR THE DEGREE

Doctor of Philosophy

APPROVED, THESIS COMMITTEE:

Paul Cloutier, Chair
Professor of Physics and Astronomy

Richard Wolf
Professor Emeritus of Physics and Astronomy

Matthew Fraser
Assoc. Professor of Civil and Envir. Engineering

HOUSTON, TEXAS

NOVEMBER 2005

Abstract

Low frequency plasma waves at Mars by

Jared R. Espley

Mars Global Surveyor's magnetometer/electron reflectometer (MAG/ER) experiment has returned over eight years of observations of low frequency plasma waves produced in the interaction of the solar wind with the Martian ionosphere. Using the MAG/ER data, I identify the properties and physical origins of the waves in the magnetosheath, magnetic pileup region, and ionosphere. I find that the waves in the dayside magnetosheath are predominately mirror mode instabilities produced by plasma temperature anisotropies arising from the draping of the solar wind magnetic field around the ionosphere. The nightside magnetosheath shows evidence for resonant ion instabilities arising from the interaction of the solar wind plasma with the ionospheric plasma. These waves are therefore an indirect observation of ongoing atmospheric loss at Mars. During the large solar storm of October 2003, dramatic changes were observed in the plasma waves present; even the normally placid tail region showed signs of significant wave activity. Coherent oscillations are observed in the ionosphere and are presumably driven by solar wind fluctuations or are associated with field line resonances along crustal fields.

Acknowledgements

Many people have assisted me during my years of school. First, I should thank Mario Acuña for providing financial support for my graduate career. My thesis advisor, Paul Cloutier, has provided energetic, insightful advice on both science and on enjoying life. Richard Wolf also offered support as a member of my committee and was always ready with patient guidance and wisdom when I would wander into his office. As one of my class instructors, Matt Fraser taught me more chemistry than I learned in all of undergrad, and as the outside committee member he willingly read my thesis despite it not having any chemistry and scarcely any atmosphere.

Many of my fellow graduate students and friends assisted me with IDL, Latex, general computer problems, proofreading, or general support. I should specifically note Scott Berger, Marcos Huerta, Carl Huffman, Dan Kocovski, Colby Lemon, and Dave Streutker. My co-authors (Paul Cloutier, Dave Brain, Dana Crider, and Mario Acuña) on the published papers related to this thesis should be acknowledged.

My parents played a tremendous role in helping me arrive to this point in my life. Besides all the support and love they've offered over the years, I'd like to especially thank my dad for introducing me to the excitement of space and my mom for introducing me to the excitement of exploring the world around me.

Lastly, I'd like to thank my dear Clau. She has supported me in so many ways through the years and I'm a better person and scientist because of her. I hope that I've been able return that support in some small portion especially as she also finishes

her PhD and our adventures together move into a new phase.

Contents

1	Introduction	1
1.1	Background information	1
1.2	A note about terminology	5
1.3	Previous work	6
2	The MGS dataset	9
3	Analysis techniques	12
3.1	Preliminary steps	12
3.2	Specific Analyses	15
3.2.1	Longitudinal, transverse, tangential, and radial amplitudes	15
3.2.2	Direction of wave vector, ellipticity	15
3.2.3	Sense of polarization	17
3.2.4	Correlation between MAG and ER data	17
3.2.5	Wavelet Analysis	18
4	General results on waves in the magnetosheath and MPR	21
4.1	General statistical results	21
4.1.1	Description of the production of the maps	22
4.1.2	600 second intervals	23
4.1.3	60 second intervals	32
4.2	Case studies	37
4.2.1	m98d101	39
4.2.2	m98d152	43
4.2.3	m98d209	46
4.3	Discussion of results	49
5	Results during the October 2003 solar storm	61
5.1	Introduction	61
5.2	Observations	63
5.3	Discussion	72
6	Initial results from the ionosphere	77
6.1	Introduction	77
6.2	Results	81
6.3	Discussion	88
7	Concluding Remarks	91

List of Figures

1.1	Mars' interaction with the solar wind	4
4.1	$\delta B/ B $ for the 600 second intervals	23
4.2	B_{\perp}/B_{\parallel} for the 600 second intervals	24
4.3	Spectral power ratio for the 1 to 10 Hz range of the 600 second intervals	25
4.4	Spectral power ratio for the 0.1 to 1 Hz range of the 600 second intervals	26
4.5	Spectral power ratio for the 0.01 to 0.1 Hz range of the 600 second intervals	27
4.6	Spectral power ratio for the 0.001 to 0.01 Hz range of the 600 second intervals	28
4.7	Wave vectors for the 600 second intervals	29
4.8	Ellipticity of the 600 second intervals	30
4.9	The relative sense of the polarization of the 600 second intervals . . .	31
4.10	The ratios of tangential and radial amplitudes for the 600 second intervals	32
4.11	Correlation between the ER and $ B $ data for the 600 second intervals	33
4.12	Correlation between the ER and B_{\parallel} data for the 600 second intervals	34
4.13	Correlation between the ER and B_{\perp} data for the 600 second intervals	35
4.14	$\delta B/ B $ for the 60 second intervals	36
4.15	B_{\perp}/B_{\parallel} for the 60 second intervals	37
4.16	Wave vectors for the 60 second intervals	38
4.17	Ellipticity of the 60 second intervals	39
4.18	The ratios of tangential and radial amplitudes for the 60 second intervals	40
4.19	Correlation between the ER and $ B $ data for the 60 second intervals .	41
4.20	Correlation between the ER and B_{\parallel} data for the 60 second intervals .	42
4.21	Correlation between the ER and B_{\perp} data for the 60 second intervals .	43
4.22	Analysis of waves for an interval in the dayside magnetosheath	44
4.23	Wavelet analysis of the B_{\parallel} component in the dayside magnetosheath .	45
4.24	Wavelet analysis of the B_{\perp} component in the dayside magnetosheath	46
4.25	An example of waves in the nightside magnetosheath	48
4.26	Wavelet analysis of the B_{\parallel} component of the nightside magnetosheath	49
4.27	Wavelet analysis of the B_{\perp} component of the nightside magnetosheath	50
4.28	An example of waves in the magnetosheath terminator	51
4.29	Wavelet analysis of the B_{\parallel} component of the magnetosheath terminator	52
4.30	Wavelet analysis of the B_{\perp} component of the magnetosheath terminator	53
5.1	Waves during decimal day 303.402 of 2003	64
5.2	Wavelet analysis of the B_{\parallel} of figure 5.1	66
5.3	Wavelet analysis of the B_{\perp} of figure 5.1	67

5.4	Waves during decimal day 303.233 of 2003	68
5.5	Wavelet analysis of the B_{\parallel} of figure 5.4	69
5.6	Wavelet analysis of the B_{\perp} of figure 5.4	70
5.7	Interval showing no unusual solar activity	71
5.8	Wave activity during decimal 303.433 of 2003	72
5.9	Wavelet analysis of the B_{\parallel} of figure 5.8	73
5.10	Wavelet analysis of the B_{\perp} of figure 5.8	74
6.1	The magnetotelluric technique	80
6.2	Ionospheric waves far from a crustal source	81
6.3	Wavelet analysis of the B_{\parallel} far from a crustal source	83
6.4	Wavelet analysis of B_{\perp} far from a crustal source	84
6.5	Ionospheric waves near a crustal source	86
6.6	Wavelet analysis of B_{\parallel} near a crustal source	87
6.7	Wavelet analysis of B_{\perp} near a crustal source	88

List of Tables

4.1	Wave properties of case examples	47
-----	--	----

Chapter 1

Introduction

1.1 Background information

Mars has fascinated humanity for millennia. In the modern age, Mars has been the focus of serious scientific inquiry for several decades. In many ways, Mars is the object in the solar system that is the most similar to our own Earth. It possesses a thin but dynamic atmosphere and its cold desert-like landscapes show evidence for wind, water, and volcanic processes. Understanding Mars as a planetary system aids in understanding our own planet. The likely future presence of human explorers on Mars provides further motivation for its study as does the tantalizing possibility of past or even present life on Mars. Despite the research done to date, much remains unknown about Mars as a planetary system. This thesis explores one such aspect of Mars, which hitherto had remained relatively unknown - that of low frequency plasma waves in the near Mars space.

Mars lacks a global intrinsic magnetic field [*Acuña et al.*, 1998], so its interaction with the solar wind is similar to the Venusian [*Cloutier et al.*, 1999] and cometary [*Mazelle et al.*, 1995] interactions. The solar wind interacts directly with these ob-

jects' ionospheres which form the principal obstacles to the flowing solar wind. Such interactions produce what are sometimes called induced magnetospheres [Luhmann *et al.*, 2004], which share some characteristics with intrinsic magnetospheres such as the Earth's or Jupiter's but also demonstrate significant differences. In the case of Mars, patches of the Martian crust are highly magnetized and also contribute to standing off the solar wind by the creation of mini-magnetospheres [Acuña *et al.*, 1998]. For the strongest crustal fields, the mini-magnetospheres protrude above the ionopause [Brain *et al.*, 2003] and protect the atmosphere that lies below them just as the Earth's global magnetosphere protects the terrestrial atmosphere from the solar wind. In all cases, such induced magnetospheres produce a variety of plasma boundaries and fluctuations as the solar wind plasma streams past plasma created from the atmospheres of the objects.

In general, the main boundary produced is a bow shock where the supersonic solar wind is slowed as it is diverted around the obstacle created by the ionosphere. Additional boundaries are commonly produced downstream of the shock. In the case of Mars, one such boundary is the magnetic pileup boundary (MPB) which was identified by Vignes *et al.* [2000] using data from the Mars Global Surveyor (MGS) Magnetometer/Electron Reflectometer (MAG/ER) investigation [Acuña *et al.*, 1998]. This boundary is the same boundary as the planetopause reported by Trotignon *et al.* [1996] using Phobos 2 data. Similar boundaries have been identified at comets [Neubauer *et al.*, 1986] and at Venus [Bertucci *et al.*, 2003]. The region between the

bow shock and MPB is called the magnetosheath (sometimes abbreviated MS). The region below the MPB is called the magnetic pileup region (MPR) and has its lower boundary in the photo-electron boundary (PEB), where the majority of the electron spectra are characteristic of electrons of planetary origin and which is, therefore, probably associated with the ionopause [Mitchell *et al.*, 2000]. A region sometimes called the tail or magnetotail is present on the nightside below the MPB, although a distinct boundary between the nightside MPR and the tail has not been identified. Figure 1.1 shows a schematic diagram (approximately to scale) illustrating the regions and boundaries just enumerated. The solar zenith angle (SZA) measures the angle from the Mars-Sun line shown in figure 1.1.

Besides plasma boundaries, magnetic and plasma disturbances are important and common features created by solar wind interactions. As will be explored in more detail later in this thesis, such phenomena are interesting for a number of reasons. In a collisionless plasma (such as the solar wind and some regions of ionospheres) these fluctuations act as a key method of redistributing energy in the system. Understanding the waves modes present allows indirect probing of the physical plasma properties such as the particle pressure, the magnetic pressure, number density, and temperature. At Mars, they are related to pickup ion processes and are therefore important to studies of atmospheric loss and climate change [Jakosky and Phillips, 2001]. Studying these fluctuations is important in order to understand the energetic particle environment at both the surface and in space (“space weather”), and to understand

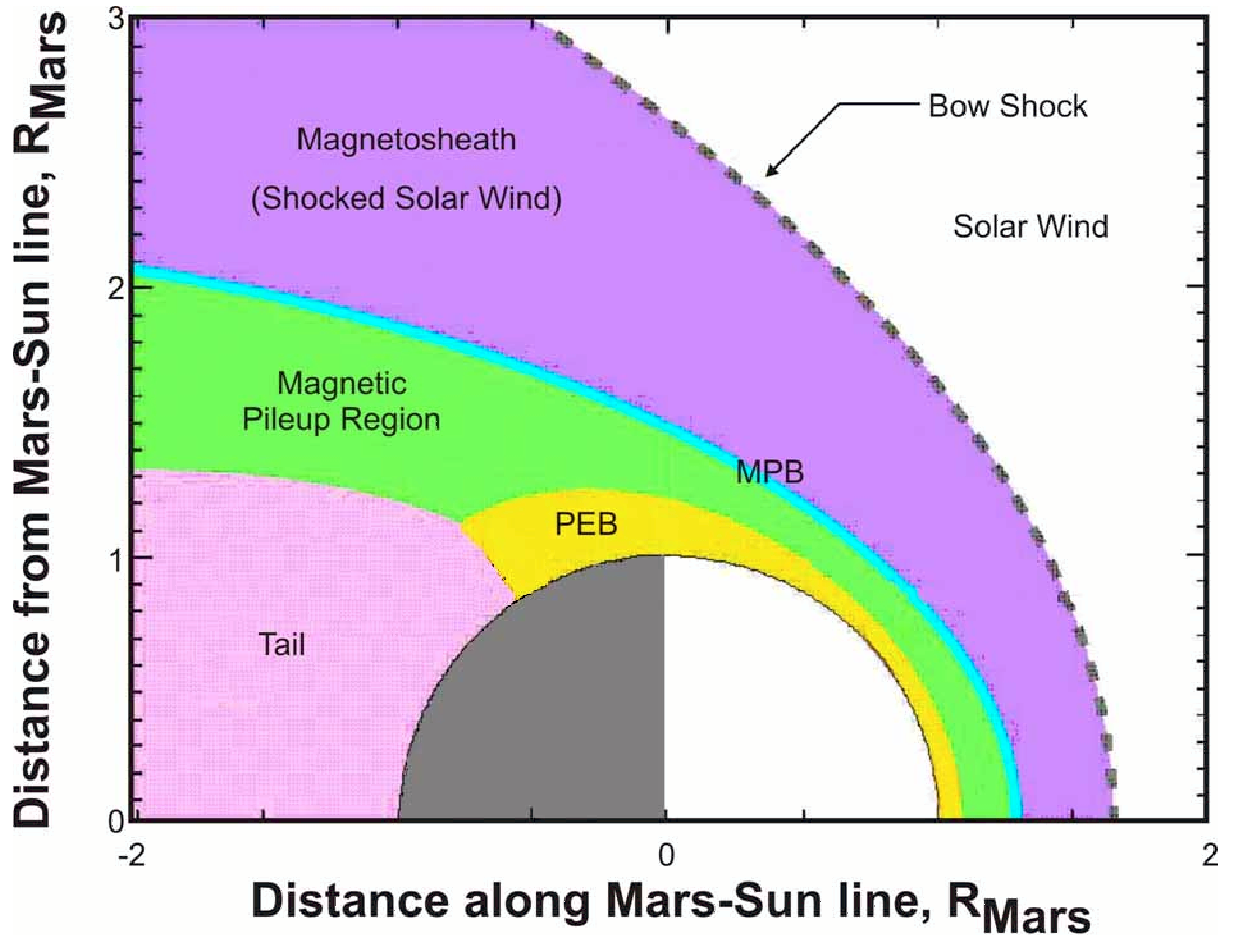


Figure 1.1: A schematic diagram (approximately to scale) illustrating the regions of the Martian interaction with the solar wind. Not shown are the complications introduced by the crustal magnetic field sources. The MPB is the magnetic pileup boundary and the PEB is the photo-electron boundary. Adapted from *Crider et al* [2003].

the origin of low frequency electromagnetic signals detectable at the surface.

This thesis uses data returned from the MGS MAG/ER investigation to observe low frequency plasma waves in the Mars system and attempts to identify the physical origin and implications of these waves.

1.2 A note about terminology

Traditionally, in space plasma physics, the term low frequency (LF) refers to fluctuations at about the natural frequencies of a plasma (such as the plasma frequency or the ion gyrofrequency). The term ultra-low frequency (ULF) has been used to refer to frequencies below the dominant local ion gyrofrequency. This usage stands in contrast to the terminology employed in a common plasma physics handbook, the NRL Plasma Formulary [*Huba, 1998*]. There, ULF waves are defined as having frequencies less than 30 Hz and LF waves as having frequencies between 30 and 300 kHz.

It is also common in space plasma physics to refer to ULF waves as magnetohydrodynamic (MHD) waves regardless of whether the theory of magnetohydrodynamics or a kinetic based theory (such as Vlasov theory) is used to describe them. Likewise, the term plasma waves is sometimes used to mean only waves near the plasma frequency of the plasma.

In this thesis, I use the term low frequency to refer to all fluctuations with frequencies near and below the local ion gyrofrequency. I also reserve the term magnetohydrodynamics for the theory and do not use it to refer to any particular frequency range. Likewise, when I use the term plasma waves I refer simply to waves in a plasma and am not referring to a particular frequency band.

I use the terms waves and oscillations more or less interchangeably to mean varying quantities that have periodic structure. The terms fluctuation and perturbation are usually used more broadly to refer to quantities that are changing which may or may

not be periodic. Instability is generally used to refer to variations that are not clearly periodic but that grow in amplitude over time.

1.3 Previous work

Studies of terrestrial low frequency magnetic waves started as early 1861 by Balfour Stewart when he recorded magnetic fluctuations that he correctly ascribed to currents in the ionosphere [Kivelson, 1995]. Work continued in the subsequent decades but the field made rapid progress with the advent of the space age in the 1950s. Numerous near Earth probes explored the Earth's magnetosphere and produced a wealth of information about low frequency plasma waves which allowed theories to be constructed that connected the observations on the ground with the observations made in space. Several review articles provide an overview of the modern state of the field [Gary *et al.*, 1993; Hubert, 1994; Omid *et al.*, 1994; Lacombe and Belmont, 1995; Kivelson, 1995; Schwartz *et al.*, 1996].

Using data from a variety of interplanetary probes, studies of low frequency plasma waves have been done for most objects in the solar system, though with unequal degrees of completeness. We focus here on reviewing previous work on Mars itself and other similar unmagnetized obstacles to the solar wind.

Huba and Strangeway [1997] summarize in a review article much of the current understanding of plasma waves at Venus. Plasma waves have been found across many frequency ranges and the observations include waves observed both upstream of the

bow shock and in the regions between the bow shock and the ionosphere. At the low frequency (LF) range however, comparatively little work has been done, especially downstream of the bow shock. *Strangeway and Crawford* [1995] and *Orlowski et al.* [1990] identified some LF oscillations in the region upstream of the Venusian bow shock, and *Orlowski et al.* [1994] were able to compare such oscillations to specific wave modes predicted by linear Vlasov theory and Hall-MHD theory. *Brace et al.* [1983] were able to identify LF waves in the nightside ionosphere of Venus. *Luhmann et al.* [1983] determined that LF fluctuations in the Venusian magnetosheath could be associated with fluctuations at the shock that are convected into the magnetosheath. *Winske* [1986] offered an alternative explanation associating the fluctuations with beam instabilities created by the interaction of the solar wind with newly born ions of planetary origin. *Luhmann et al.* [1987] examined the role of plasma fluctuations and quasi-parallel shocks on pickup ion escape. Recent work by *Grebowsky et al.* [2003] identifies LF waves associated with pickup ions in the Venusian ionosheath.

LF waves at comets have received more study. Several review papers lay out the basic theory and observations of LF waves at comets [*Lee*, 1989; *Ip and Axford*, 1990; *Tsurutani*, 1991a; *Tsurutani*, 1991b]. Several papers report observations made of LF waves both upstream of cometary bow shocks and downstream in the cometary magnetosheaths and the magnetic pileup regions [*Tsurutani and Smith*, 1986a,b; *Glassmeier et al.*, 1987; *Mazelle et al.*, 1991; *Glassmeier and Neubauer*, 1993; *Glassmeier et al.*, 1993; *Neubauer et al.*, 1993].

At Mars, detailed observations of plasma waves started with the Soviet spacecraft Phobos 2 [*Riedler et al.*, 1989; *Grard et al.*, 1989; *Sagdeev et al.*, 1990]. LF waves near the proton gyrofrequency have been observed upstream of the Martian bow shock using both Phobos 2 data [*Russell et al.*, 1990; *Russell et al.*, 1992; *Sauer et al.*, 1998a; *Tarasov et al.*, 1998; *Delva and Dubinin*, 1998] and MGS data [*Brain et al.*, 2002; *Sergis and Moussas*, 2002]. Initial reports of LF waves within the magnetosheath and the magnetic pileup region have also been made using Phobos 2 data [*Sauer et al.*, 1998b] and MGS data [*Cloutier et al.*, 1999; *Crider*, 1999; *Bertucci et al.*, 2004; *Bertucci*, 2003; *Grebowsky et al.*, 2003]. Work on the magnetohydrodynamic theory of bi-ion plasma waves with specific application to Mars has been carried out by *Sauer et al.* [1997; 1999; 2001]. *Winningham et al.* [2005] used data from the electron spectrometer aboard Mars Express to characterize fluctuations in the electron fluxes in the near Mars space.

Lastly, my co-authors and I have published work using MGS data to characterize in detail the magnetic fluctuations in the magnetosheath [*Espley et al.*, 2004], during the large solar storm of October 2003 [*Espley et al.*, 2005a], and in the ionosphere [*Espley et al.*, 2005b]. Much of this thesis replicates and expands on this previous work.

Chapter 2

The MGS dataset

MGS arrived at Mars in 1997 and since that time the Magnetometer/Electron Reflectometer (MAG/ER) investigation has been returning a steady flow of data [Acuña *et al.*, 2001]. When MGS first arrived at Mars it began a slow process of aerobraking in order to circularize its orbit. During these “pre-mapping” phases of the mission, MGS sampled a large variety of altitudes and solar zenith angles (SZAs) as its elliptical orbit was gradually brought down to the circular mapping orbit which it reached in February of 1999 [Albee *et al.*, 2001]. All data returned since that time have been from the near circular mapping orbit which has an approximate altitude of 400 km, an orbital period of 2 hours, and covers 0200 to 1400 in local time. In this thesis, I use primarily pre-mapping data (phases AB-1, AB-2, SPO1, and SPO2 [Albee *et al.*, 2001]) although occasionally I make use of mapping phase data (such as when I study plasma waves during the October 2003 solar storm).

The MAG instrument consists of two redundant triaxial vector magnetometers that provide measurements of the ambient magnetic field with a maximum data rate of 32 samples per second with a range of ± 4 nT to $\pm 65,536$ nT. The data rate varied

between 32, 16, and 8 samples per second according to the telemetry requirements of the spacecraft. Every 24th datum was recorded at its full value (“full word”) and all samples in between recorded only the difference from the last full value. This created both high (using all available samples) and low (using only the full word samples) time resolution data. Since the magnetometers were located on the solar panels, currents from some of the electronics onboard the spacecraft produced fields that were detected by the instruments. However, using a spacecraft magnetic field model developed from calibration maneuvers, the static and dynamic background has been largely removed from the low time resolution data [Acuña *et al.*, 2001]. For the high time resolution data, the dynamic background could not be subtracted because the engineering data used to calibrate the full word measurements could not be reliably interpolated to create dynamically calibrated high time resolution data. This dynamic spacecraft field is expected to vary with the spacecraft spin period of ~ 100 minutes. Furthermore, even the low time resolution data are estimated to be only reliably calibrated to within ± 3 nT. The calibration is expected to be considerably better (< 0.5 nT) for measurements made on the nightside [J. E. P. Connerney, personal communication, 2003].

For these reasons, I use the low time resolution data to calculate the magnitude of the magnetic field which I then use to calculate quantities such as the ion gyrofrequencies. I use the high time resolution data to calculate quantities that are relative to the mean magnetic field and to do spectral analysis. Thus I use the most

fully calibrated data when necessary and use the highest time resolution data when possible.

The ER instrument measures electron fluxes every 2 to 48 secs across 30 energy channels ranging from 10 eV to 20 keV in 16 geometrically separate sectors. Because I am interested primarily in the relative densities of electrons in order to compare them to the fluctuations in the magnetic field, I generally use the omni-directional flux of the electrons in just one of the energy bins (the 191 eV bin) with the highest time resolution.

The MGS data used in the study are given (prior to the data processing described below) in the Sun-state (SS) Cartesian coordinate system. In this system, the Mars-Sun line is defined as the +x direction, the orbital motion of Mars is the -y direction, and the +z axis completes the orthogonal set (and is roughly northward on Mars). This system could also be called the Mars solar orbital (MSO) system since it is comparable to the geocentric solar ecliptic (GSE) and the Venus solar orbital (VSO) coordinate systems.

Chapter 3

Analysis techniques

The central idea of this thesis is to take the time series MAG and ER data, examine and characterize the fluctuations in those data at different locations and under a variety of conditions, and compare those characteristics to various theoretical wave modes and physical models. In this section, I describe in detail my methods of characterizing the fluctuations.

3.1 Preliminary steps

The most basic step in many of the analysis methods used in this study is the determination of the mean magnetic field for a given interval. I determine the magnitude and direction of this mean field and then rotate the MAG data into a coordinate system that is aligned along this mean field (MF). In this MF coordinate system, the principal direction is defined as the direction of the mean magnetic field over some given time interval (B_{\parallel}), the second direction is perpendicular to the mean field and contains no z-component from the SS measurements ($B_{\perp 1}$), and the third direction is perpendicular to the other two directions ($B_{\perp 2}$). B_{\perp} is defined as the vector addition

of $B_{\perp 1}$ and $B_{\perp 2}$. Perturbations from the mean field can then be calculated in each of these directions for every measurement within the time interval.

Determining the appropriate length for this time interval is one of the difficult issues with this analysis method. Because the measurements are made by a moving spacecraft, one of the dangers in interpreting perturbations in observed parameters is that the spacecraft may be simply passing through a variety of plasma regimes with different characteristics rather than observing intrinsic wave structures. Conversely, if I were to use too short of a time interval I would be excluding wave modes that have characteristic periods larger than our chosen time interval. For intervals selected manually, I was able to choose intervals that do not obviously contain dramatic, global changes in the magnetic field signature (large discontinuities or steeply changing mean magnitudes). For statistical studies, where I wanted to include all possible data and manual selection of each interval was not feasible, I chose to use two interval lengths – 60 seconds and 600 seconds. In order to prevent features at the edges of particular intervals from being neglected, I incremented the start times of the intervals by 30 and 300 seconds, respectively.

Using the rule of thumb that a fluctuation needs to repeat at least three times before it can reasonably be called periodic, the analyses done with an interval of 60 seconds can be expected to reflect oscillations with frequencies as low as 0.05 Hz. Based on the observed magnetic field magnitude in the near Mars space of order 10 nT, the expected order of magnitude of the proton gyrofrequency should be 0.1 Hz.

Thus it is plausible that an interval of 60 seconds will capture fluctuations associated with proton gyromotion. Furthermore, given the MGS speed of approximately 5 km/s then MGS will have travelled about 300 km in the interval. This distance is significantly smaller than most of the major regions in the near Mars space.

An interval of 600 seconds however spans a distance of approximately 3000 km which is approximately one Mars radius and would potentially allow MGS to cross into different plasma regions during the interval (e.g. passing from the bow shock all the way across the magnetosheath at low solar zenith angles). However, a 600 second interval allows frequencies as low as 0.005 Hz to be sampled. This range includes the expected oxygen gyrofrequency of order 0.01 Hz. Thus, I include this interval range in my analyses despite its large spatial extent because of the possibility of detecting waves associated with ions of planetary origin.

As one last step in this initial process, I remove any large scale trends in the transformed vector components (up to third order polynomials) since these types of long period changes are the type of trends I am trying to avoid by choosing a sufficiently short time interval. All this preliminary work then allows me to perform a variety of analyses as described below.

3.2 Specific Analyses

3.2.1 *Longitudinal, transverse, tangential, and radial amplitudes*

In order to determine whether the waves were predominately longitudinal (i.e. compressional like a sound wave) or transverse (like a plucked guitar string) I calculated the average amplitude of the perturbations in the direction perpendicular to the mean field (δB_{\perp}) and in the perturbations parallel to the mean field (δB_{\parallel}). In order to measure the size of the amplitude of each “peak to valley”, I found all points of local maximum or minimum by finding all points that were either greater (or smaller) than the previous three and following three data points. Taking all these local extrema together allows me to calculate the mean value for the average amplitude of the each of the magnetic field components for the interval.

In a similar fashion, I am able to calculate the amplitudes of the fluctuations parallel to the planetary surface (i.e. tangential or horizontal) and those perpendicular to this plane (i.e. radial or vertical).

3.2.2 *Direction of wave vector, ellipticity*

In order to possibly find the direction of the wave vector (or direction of propagation for moving structures) I use minimum variance analysis. Minimum variance analysis works by finding the direction of the minimum variance of the mean magnetic field. Mathematically, this direction is found by solving for the eigenvector associated with the minimum eigenvalue of the covariance matrix [*Sonnerup and Cahill,*

1967; Means, 1972; McPherron *et al.*, 1972; Arthur *et al.*, 1976; Song and Russell, 1999]. Basically, one finds the axes of the three dimensional variance ellipsoid for a given interval of magnetic field measurements. Each axis of the variance ellipsoid is an eigenvector of the covariance matrix. The direction of the minimum eigenvalue eigenvector is then assumed to be the direction of propagation of the wave (or in the case of stationary structures to be the direction of the wave vector) which is a valid assumption for wave modes such as the standard MHD wave modes (Alfvén, fast, and slow magnetosonic waves) since these wave modes have variations that are always perpendicular to the direction of propagation. Likewise, this method assumes planarity of the waves and also assumes that one major wave mode dominates such that the wave vector direction determined is of that mode. Additionally, this method of determining the wave vector does not work well for waves with nearly linear polarization since the minimum and intermediate eigenvalues are very similar in such a case [Song and Russell, 1999; Knetter *et al.*, 2003; Hausman *et al.*, 2004]. Because of these assumptions and caveats, it is important to view with caution any results from MVA analysis, although I retain my results here as first order approximations for the direction of propagation.

I am also able to calculate the ellipticity of the ellipse produced by the eigenvectors of the largest two eigenvalues of the covariance matrix (cf. eqn. 3.4b of Song and Russell, [1999]). That is to say, I find the ellipticity of the fluctuations perpendicular to the direction of propagation for the wave. Using this analysis, an ellipticity of 1

represents a perfectly circularly polarized wave, whereas an ellipticity of 0 represents a perfectly linearly polarized wave.

3.2.3 *Sense of polarization*

Using the data in the MF coordinate system, I am able to calculate the relative mean sense of polarization for a given interval. In other words, I calculate which direction B_{\perp} is rotating around the mean field – counter clockwise (right handed like an electron) or clockwise (left handed like an ion). In order to calculate this, I simply add one every time the B_{\perp} vector moved counter clockwise and add negative one every time it moves clockwise and then normalize by the number of data in the interval. This gives me a value for the relative average sense of polarization in the interval ranging from 1 (entirely right handed) to -1 (entirely left handed). This is similar to the difference in phase shift calculation suggested by *Rankin and Kurtz* [pg. 5452, 1970].

3.2.4 *Correlation between MAG and ER data*

Another analysis technique that I use is the comparison of fluctuations in the magnetic field to the fluctuations in the ER flux data. Since I am interested mainly in any correlations between plasma density variations and magnetic field flux variations, I want to use a measurement of electron flux that best represents the general plasma characteristics. Because of this, I use the omni-directional flux of 191 eV electrons since this energy bin has the highest datarate of the available bins and is also near the

center of the observed spectral energy distribution [Mitchell *et al.*, 2001]. I first find the relative fluctuations in flux of the 191 eV electrons for a given interval. As with the magnetic field data, I cubically detrend the data to remove undesired large scale changes. I then find the Spearman correlation coefficients between these fluctuations and the fluctuations in B_{\parallel} and the B_{\perp} components. The Spearman coefficient is a nonparametric correlation coefficient that is 1 if the two time series are perfectly correlated, 0 if they are perfectly non-correlated, and -1 if they are perfectly anti-correlated [Press *et al.*, 1992]. Because of the much lower time resolution of the ER data (which is at best 8 times lower resolution than the MAG data), any correlations found represent only the lower frequencies fluctuations even for the shorter (i.e. 60 sec) intervals.

3.2.5 Wavelet Analysis

I use wavelet analysis to analyze the frequency domain of the oscillations. Wavelet analysis is similar to the technique of the windowed Fourier transform in that it can transform a signal in the time domain into a time resolved signal in the frequency domain. This allows both techniques to resolve signals in the frequency domain that are nonstationary (i.e. time varying). Wavelet analysis has the further advantage that the scalability of the wavelet basis functions allows higher time resolution at the higher frequencies of the frequency domain where it is needed, and lower time resolution at the lower frequencies. Torrence and Compo [1998] provide a clear introduction to wavelet analysis and its application to geophysical signals. In my analysis I use

the Morlet wavelet with a wave number of six because its shape gives good time localization. Also, because frequency domain analyses are especially vulnerable to false wave signals arising simply from the spacecraft motion through different plasma regimes, I pass the transformed data (which had already been cubically detrended as noted earlier) through a low pass filter specific to the region of a given interval. I attempt to have the filter remove signals that would complete 3 oscillations in the time it would take MGS to cross a spatially significant distance given the average MGS speed in the region. For intervals starting outside the bowshock, I set an acceptable distance of 2000 km (about 2/3 of a Mars radius - cf. fig. 1.1) which produces a filter that reduces spectral power below 0.0045 Hz. For intervals starting in the magnetosheath, I set an acceptable distance of 750 km which results in a filter of 0.02 Hz. Below the MPB, I use an acceptable distance of 500 km which results in a filter of 0.06 Hz. This digital filter reduces but does not remove entirely spectral power below these frequencies. I use this procedure to wavelet transform $|B|$, $B_{||}$, and B_{\perp} . The data rates of the instruments sometimes shifted according to the telemetry configuration of the spacecraft, and since such changes can produce spurious signals in the frequency domain, I also remove intervals that contain data rate changes.

Using such filtered data, I am then able to find the mean peak frequency (i.e. that frequency showing the greatest spectral power) for a given time interval in each of the following frequency intervals: 1 to 10 Hz, 0.1 to 1 Hz, 0.01 to 0.1 Hz, and 0.001 to 0.01 Hz (for 600 second intervals only). Generally, for most intervals, spectral

power decreases from the lowest to highest frequencies so I expect to see the greatest spectral power at the lowest frequencies of each frequency range. Any intervals in which the peak frequency is above the minimum for the frequency interval indicates something physically interesting is occurring there and I note that interval and peak frequency.

For these same frequency intervals, I am also able to calculate the total spectral power for a given time interval. This allows me to compare the total spectral power for the interval for B_{\parallel} and B_{\perp} . This provides an alternative measure (see section 3.2.1) of whether the waves are predominately longitudinal or transverse and allows this determination to be made for oscillations that fall within a given frequency interval.

Chapter 4

General results on waves in the magnetosheath and MPR

I present in this chapter the results from the analyses described in the previous chapter. Using data from nearly all pre-mapping orbits, I start first with general statistical results on the properties of the oscillations found in various regions of near Mars space. I then present individual intervals exhibiting interesting characteristics or features.

4.1 General statistical results

One of the questions I am interested in answering is what are the most common characteristics of low frequency plasma waves in the near Mars space? For example, if I were to go to the dayside magnetosheath of Mars right now, what would be the type of plasma waves I would be most likely to encounter? By constructing maps of the statistical occurrence of various wave characteristics I attempt to answer these questions. When viewing these general results, it is important to remain cognizant of the tremendous variety in the characteristics of individual orbits. However, these

general results provide a benchmark by which we can examine the individual orbits.

4.1.1 Description of the production of the maps

Statistical maps of the most likely characteristics for various wave parameters are shown in the sections below. I describe in this subsection the process involved in creating these maps. First, taking results from the analyses described in the previous chapter I bin all data within two standard deviations of the mean into approximately 20 data bins. Then I find the bin with the largest amount of data, a value I call the “mode” although it clearly is not the true mode of the distribution. Using this mode, I find the most likely value for each location in the near Mars space based on all data from intervals that originated from that location. To depict these locations, I use the SS or MSO coordinate system described in chapter 2. On the x-axes of the maps, I plot the distance along the Sun-Mars line and along the y-axes, the distance away from this line. In order to give some indication of whether the location is in the southern hemisphere (where the majority of the crustal fields are) or in the northern hemisphere, I plot locations in the northern hemisphere as having a positive distance from the Mars-Sun line and those in the southern hemisphere as having a negative distance from the Mars-Sun line. I use a grid of spatial bins of 0.2 by 0.2 Mars radii where the Martian radius is approximately 3396 km. On this spatial grid I fill each box with a color corresponding to the “mode” for that location. I also plot the location of Mars and the best-fit average locations of the MPB and bow shock [*Vignes et al.*, 2000].

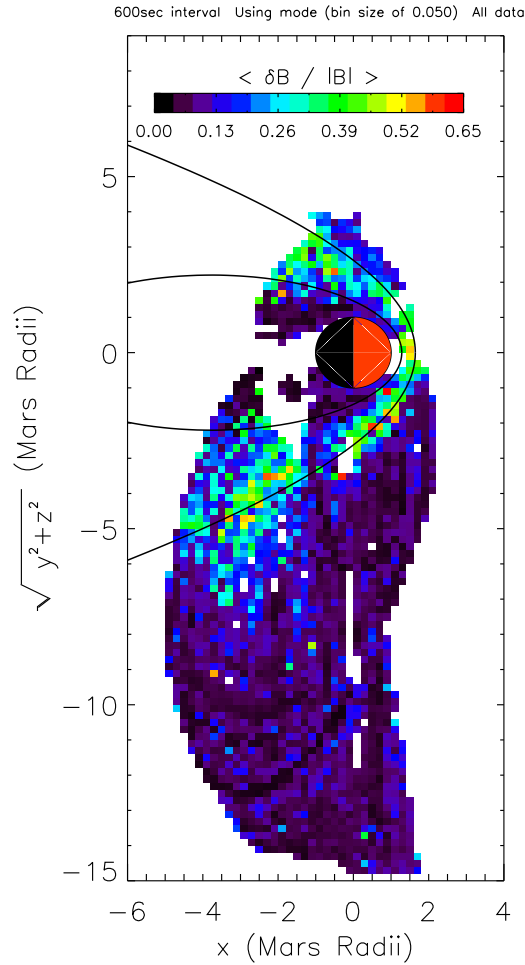


Figure 4.1: The average amplitude of the fluctuations divided by the magnitude of the magnetic field for the 600 second intervals.

4.1.2 600 second intervals

The first statistical result I show is in figure 4.1. There the average amplitude of the fluctuations (δB) normalized by $|B|$ is shown. Strong, often nonlinear, fluctuations are clearly present throughout the magnetosheath.

Figure 4.2 shows the map of the base 10 logarithm of the B_{\perp} average fluctuations divided by the B_{\parallel} average fluctuations for the intervals of 600 seconds. Colors toward the blue end represent intervals of predominantly compressional waves whereas colors

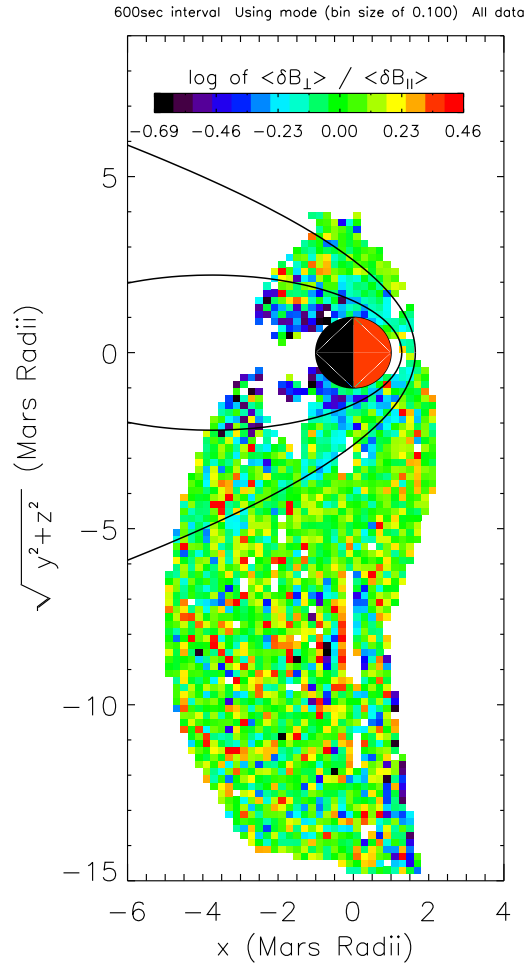


Figure 4.2: The \log_{10} of the B_{\perp} average fluctuations divided by the B_{\parallel} average fluctuations for 600 second intervals.

toward the red indicate the predominance of transverse fluctuations. The areas of green color are regions that, on average, have predominance of neither direction. The fluctuations in the dayside magnetosheath and MPR are predominantly compressional whereas most other regions show an approximately equal mix. Note that this method of measuring the amplitudes of the fluctuations is most sensitive to the lower frequency fluctuations (see chapter 3).

Figures 4.3, 4.4, 4.5, and 4.6 show an alternative method to determine the com-

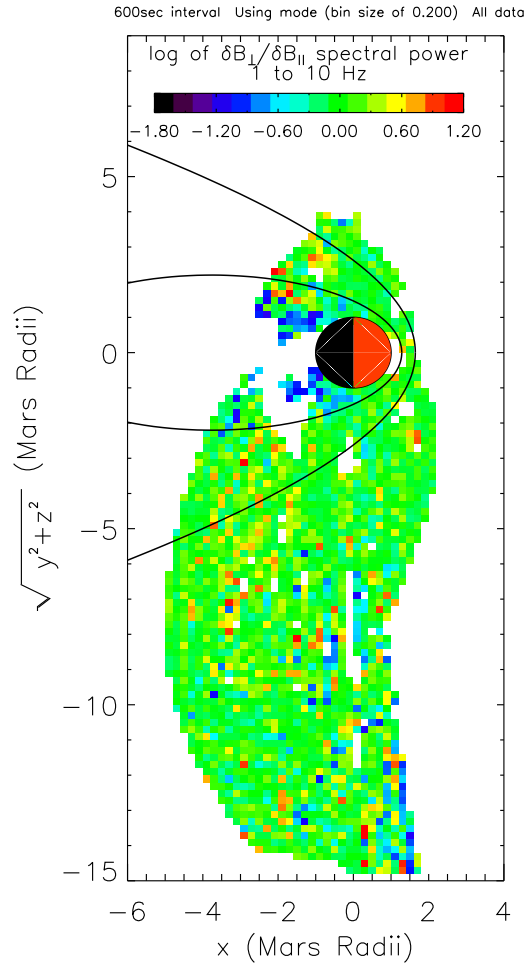


Figure 4.3: The \log_{10} of the spectral power ratio of the B_{\perp} average fluctuations and the B_{\parallel} average fluctuations for 1 to 10 Hz range for the 600 second intervals.

pressional versus transverse nature of the waves. They show the base 10 logarithm of the ratio of B_{\perp} and B_{\parallel} fluctuations for, respectively, frequencies between 1 and 10 Hz, 0.1 and 1 Hz, 0.01 Hz and 0.1 Hz, and 0.001 and 0.01 Hz. The color scheme is qualitatively the same. Figure 4.3 shows that the highest observable frequency fluctuations in the dayside magnetosheath and MPR are more evenly distributed between compressional and transverse power. Figures 4.4, 4.5, and 4.6 show that the compressional power in the dayside magnetosheath increases proportional to the tran-

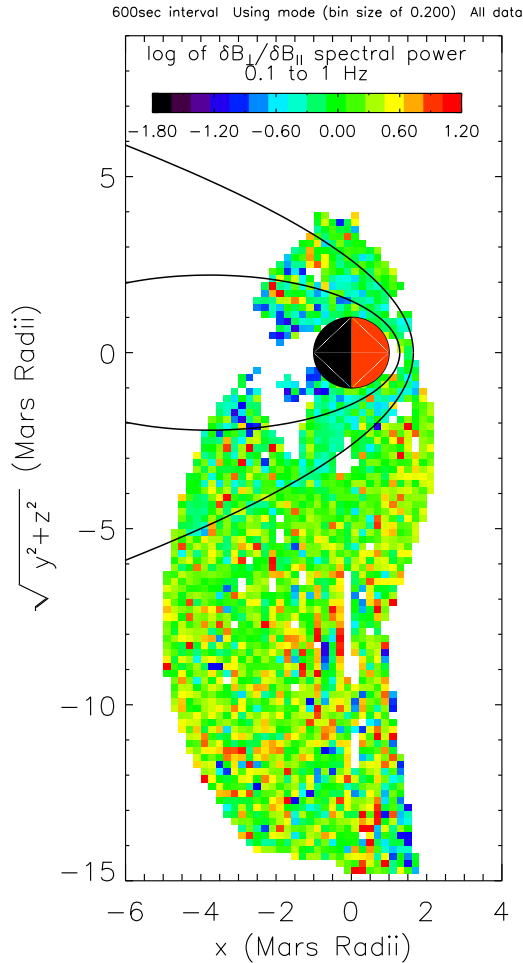


Figure 4.4: The \log_{10} of the spectral power ratio of the B_{\perp} average fluctuations and the B_{\parallel} average fluctuations for 0.1 to 1 Hz range of the 600 second intervals.

verse power as one examines lower and lower frequencies. This result is consistent with figure 4.2. Also of interest are the hints of transverse power in the nightside magnetosheath in all frequency regimes, although these intervals of transverse are mixed intervals of compressional power.

Figure 4.7 shows the average wave vectors (or directions of propagation for non-stationary structures) relative to the mean field. Only those intervals that had ratios 3 or greater for the intermediate to minimum eigenvalues of the MVA analysis are

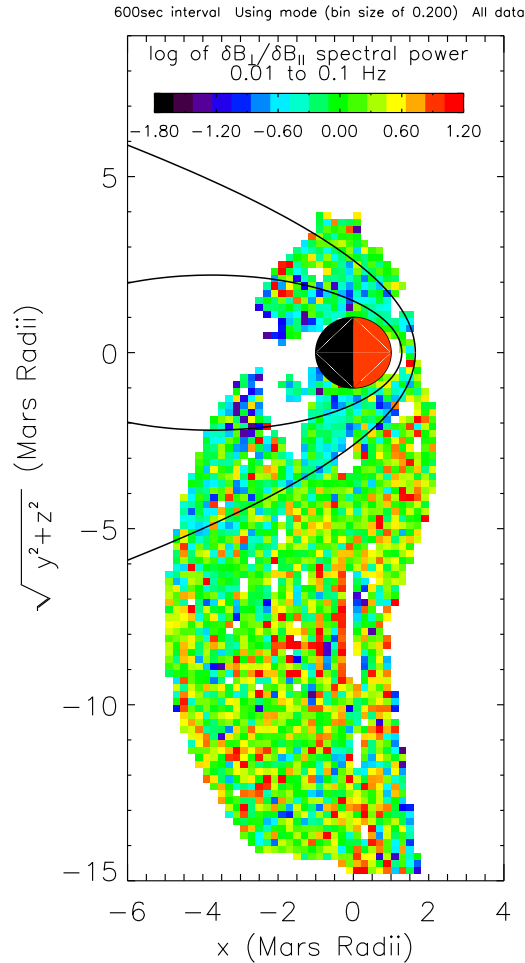


Figure 4.5: The \log_{10} of the spectral power ratio of the B_{\perp} average fluctuations and the B_{\parallel} average fluctuations for 0.01 to 0.1 Hz range of the 600 second intervals.

shown. This condition resulted in only about half (24,879 of 52,355) of all available intervals being used. It is obvious that most waves are propagating nearly perpendicular to the mean field throughout the magnetosheath. However, in the outer portions of the nightside magnetosheath the directions become more mixed and as one moves out into the region beyond the shock, the wave vectors become more nearly parallel to the mean field. As with most the analyses in this section, these results are somewhat dependent on the size of the interval chosen to analyze and hence these results are

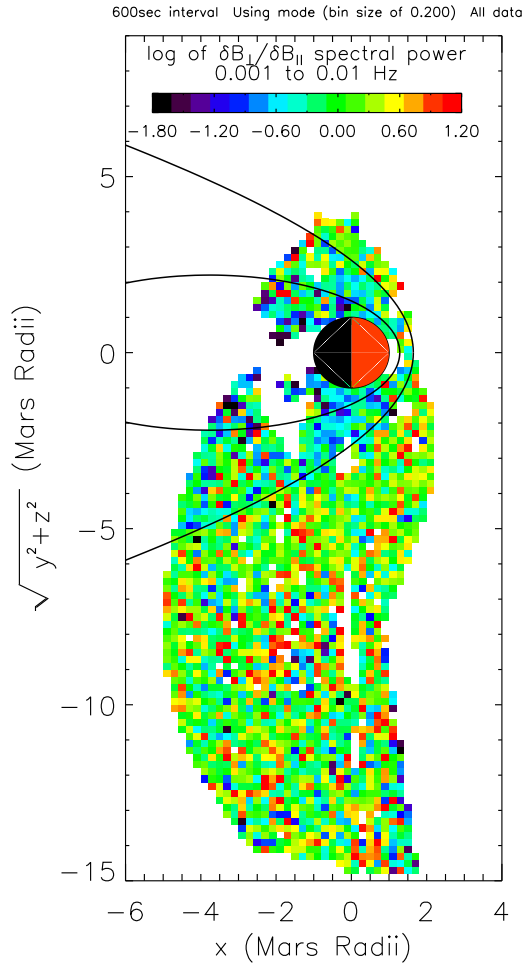


Figure 4.6: The \log_{10} of the spectral power ratio of the B_{\perp} average fluctuations and the B_{\parallel} average fluctuations for 0.001 to 0.01 Hz range of the 600 second intervals.

most applicable to the lowest frequency fluctuations measured.

Figure 4.8 shows the ellipticity of the fluctuations in the directions of maximum and intermediate variance. An ellipticity of 1 represents perfectly circular polarization whereas an ellipticity of 0 represents perfectly linear polarization. Most of the fluctuations in the magnetosheath are moderately elliptical with the ones in the night-side magnetosheath increasing toward greater circularization. Any fluctuations in the magnetotail and far upstream of the shock are generally relatively linearly polarized.

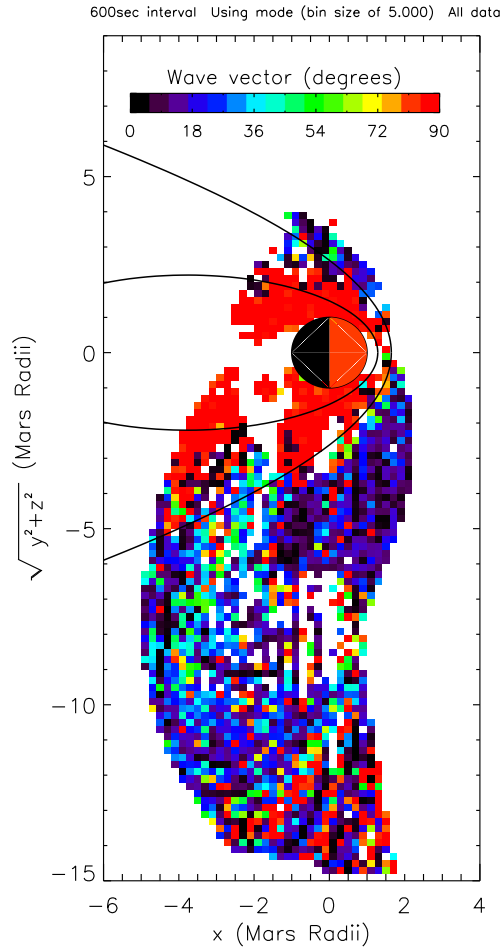


Figure 4.7: The wave vector (angle of propagation) relative to the mean field for the predominant wave form of the interval. Only intervals that have ratios of 3 or greater for the MVA intermediate and minimum eigenvalues are included.

These results are especially dependent on the lowest frequency fluctuations.

The relative sense of polarization of the B_{\perp} components is shown in figure 4.9. The handedness of the fluctuations seems to be a fairly uniform mix throughout all regions but these results may be skewed by the fact we are observing in the spacecraft frame which may be moving respect to the plasma frame which itself may be moving with respect to any propagating waves.

The ratios of the tangential (or horizontal with respect to the planetary surface)

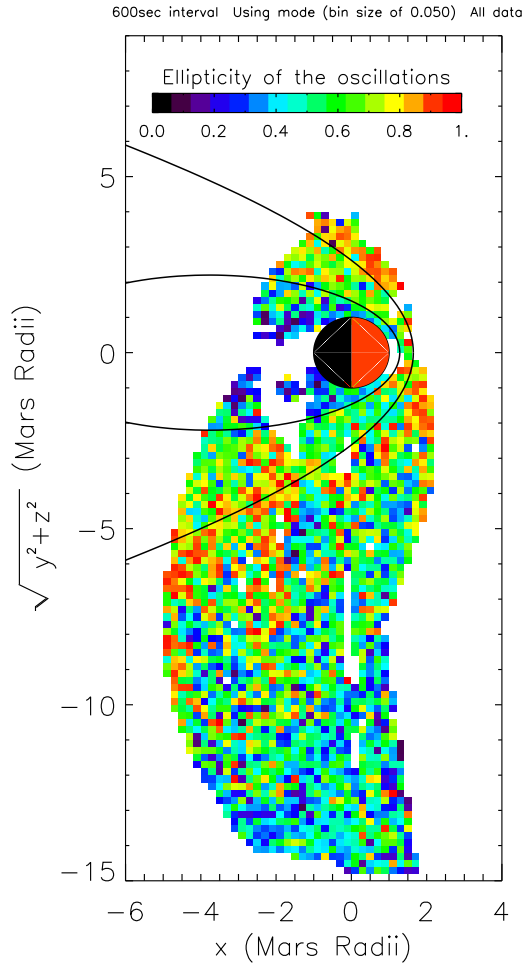


Figure 4.8: The ellipticity of the components in the directions of maximum and intermediate variance. An ellipticity of 1 represents perfectly circular polarization whereas an ellipticity of 0 represents perfectly linear polarization.

and radial (or vertical) amplitudes are shown in figure 4.10. Throughout most of the magnetosheath the ratios are about equal. In the lower parts of the dayside magnetosheath and especially in the northern hemisphere of the MPR, the horizontal amplitudes are larger. The opposite seems to be true in the far nightside magnetosheath.

Figures 4.11, 4.12, and 4.13 show the correlation coefficients between the 191 eV electron flux and, respectively, the $|B|$ fluctuations, the B_{\parallel} fluctuations, and the

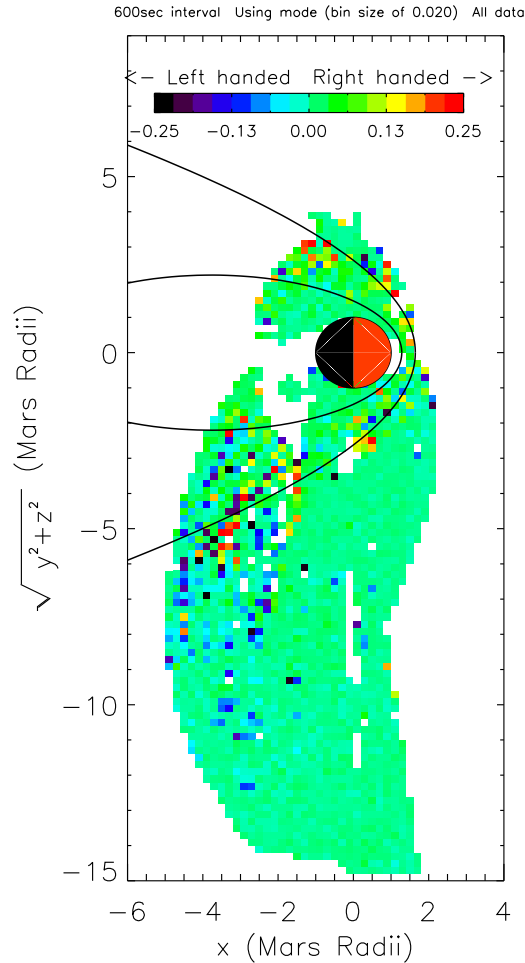


Figure 4.9: The relative sense of polarization for the 600 second intervals. Bluer colors are representative of left handed polarization being more likely and redder colors indicate that right handed polarization is more likely.

B_{\perp} fluctuations. A coefficient of 1 represents a perfect correlation, a coefficient of 0 represents no correlation at all, and a coefficient of -1 represents a perfect anti-correlation. Throughout the dayside MPR and magnetosheath, the $|B|$ fluctuations tend to be anti-correlated with the electron flux fluctuations, whereas in the nightside magnetosheath, they are clearly correlated. Figure 4.12 shows that the strongest anti-correlations for the B_{\parallel} fluctuations occur in the northern MPR. Figure 4.13 shows that the B_{\perp} are only weakly anti-correlated in the dayside MPR and magnetosheath.

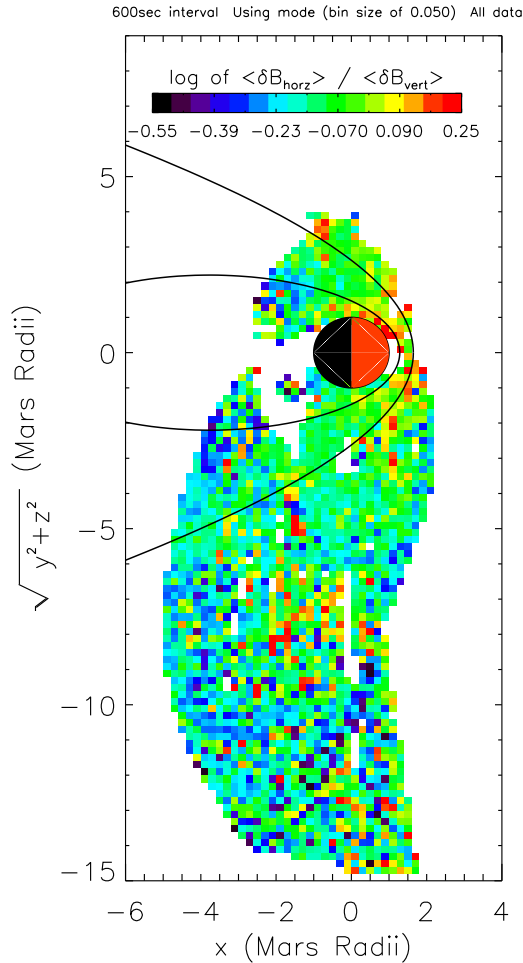


Figure 4.10: The ratios of the tangential (horizontal relative to the planetary surface) and radial (vertical) amplitudes for the 600 second intervals.

4.1.3 60 second intervals

Turning now to the analyses done for intervals of 60 seconds, it is apparent that the results are generally similar to those for the 600 second intervals although there are some differences. Figure 4.14 shows that the fluctuations are still largest in the magnetosheath but in this case they are more likely to be linear (e.g. $\delta B/|B| \lesssim 0.10$). Figure 4.15 shows that the fluctuations in the dayside magnetosheath and MPR still tend towards compressional power although less dramatically than in the case for the

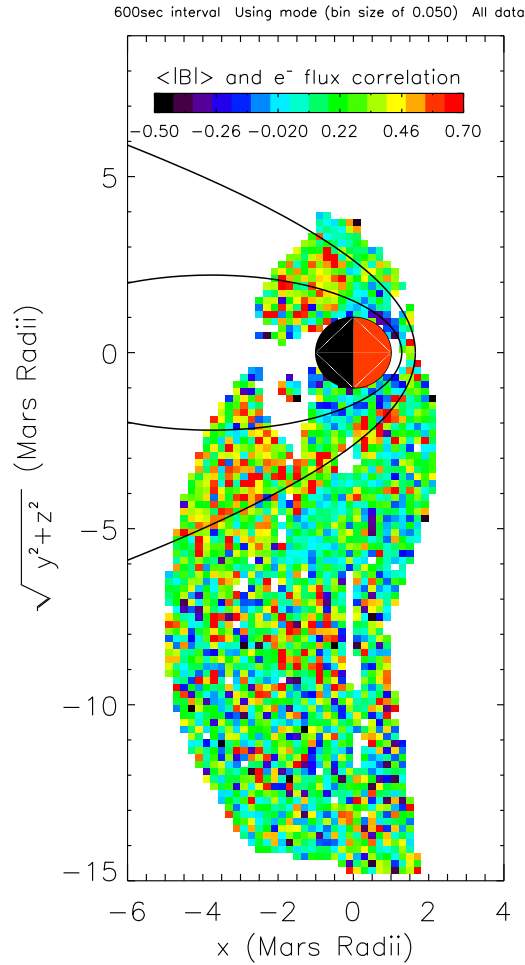


Figure 4.11: The correlation coefficient between the 191 eV electron flux and the $|B|$ data for the 600 second intervals. A coefficient of 1 represents a perfect correlation, a coefficient of 0 represents no correlation at all, and a coefficient of -1 represents a perfect anti-correlation.

600 second intervals. Other regions show a relatively even mix of compressional and transverse power. Unfortunately, because of the relatively few data points contained in the 60 second intervals, these intervals proved to be too short produce reliable wavelet transforms except for those periods in which the instruments were operating at their highest data collection rates. The resulting intervals are too sparse to make very uniform maps and hence I omit them.

Figure4.16 shows the wave vector for the dominant wave mode for those intervals

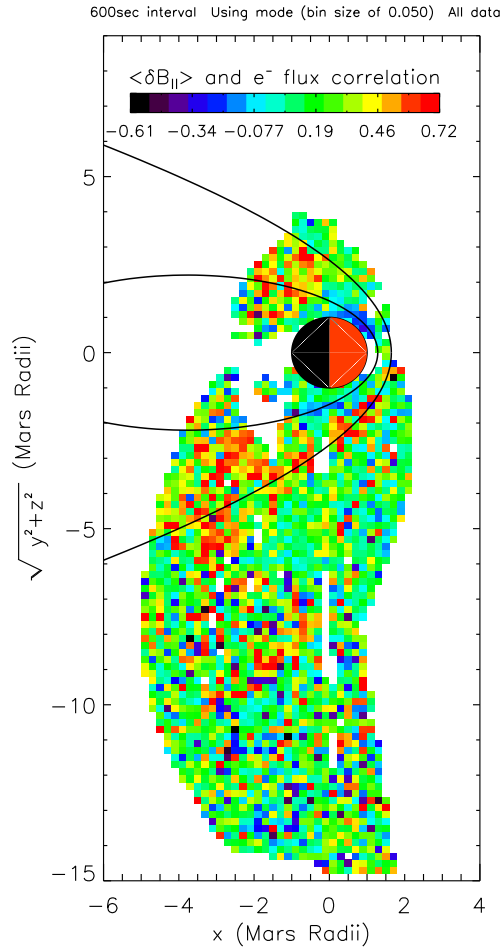


Figure 4.12: The correlation coefficient between the 191 eV electron flux and the $B_{||}$ data for the 600 second intervals. A coefficient of 1 represents a perfect correlation, a coefficient of 0 represents no correlation at all, and a coefficient of -1 represents a perfect anti-correlation.

(about half) that had MVA intermediate to minimum eigenvalue ratios of 3 or greater. The results are very similar to figure 4.7. The ellipticity of the fluctuations is shown in figure 4.17. Again, the results are similar to those for the 600 second intervals. The senses of polarization are nearly equally distributed between left and right handed, as they were for the 600 second intervals, and hence I do not show the map of this uniform distribution. Figure 4.18 shows the ratio of the tangential and radial oscillations. Continuing the trend, the results are similar to figure 4.10 although some

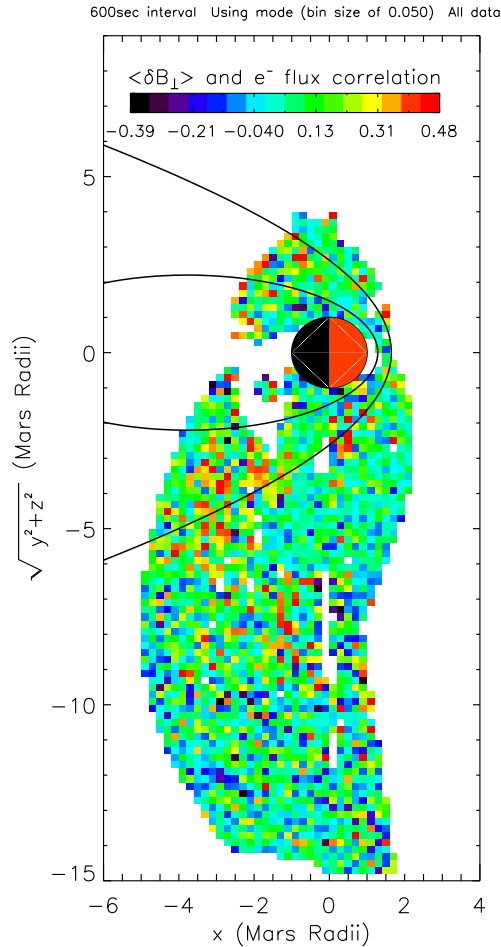


Figure 4.13: The correlation coefficient between the 191 eV electron flux and the B_{\perp} data for the 600 second intervals. A coefficient of 1 represents a perfect correlation, a coefficient of 0 represents no correlation at all, and a coefficient of -1 represents a perfect anti-correlation.

difference do appear. The trend towards larger tangential fluctuations in the dayside magnetosheath and MPR is more pronounced in the 600 second intervals; in the 60 second intervals only within the MPR does a significant inclination towards tangential oscillations appear.

Figures 4.19, 4.20, and 4.21 show the correlation coefficients for the electron flux data and the magnetic field magnitude and time series. The maps are less complete than the ones for the 600 second intervals because the shorter interval often did not

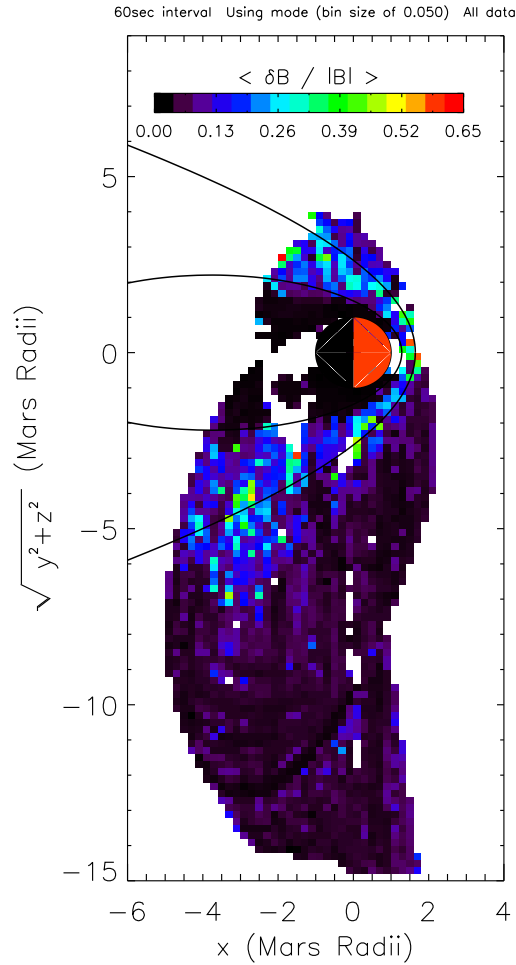


Figure 4.14: The average amplitude of the fluctuations divided by the magnitude of the magnetic field for the 60 second intervals.

allow sufficient ER data to be collected to make a correlation analysis. However, there is still enough data to see that there is still an anti-correlation between the electron flux fluctuations and the $|B|$ fluctuations in the dayside magnetosheath (figure 4.19). However, figure 4.21 shows that there is relatively little correlation in the B_{\perp} component but that the B_{\parallel} component (figure 4.20) does have a correlation, especially in the southern hemisphere (where most of the crustal fields are). This is different from the 600 second intervals where the B_{\parallel} were more likely to be anti-

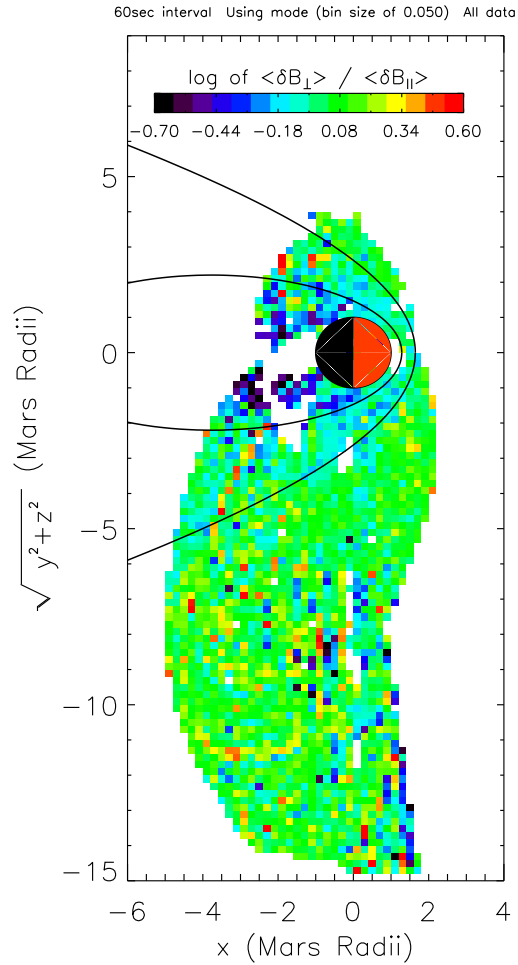


Figure 4.15: The \log_{10} of the B_{\perp} average fluctuations divided by the B_{\parallel} average fluctuations for 60 second intervals.

correlated in the northern hemisphere and the B_{\perp} component showed some, albeit small, anti-correlations.

4.2 Case studies

In order to more fully understand the general statistical results presented in the previous section, I present several example intervals that illustrate many of the characteristics just identified statistically. Many tens of thousands of other intervals are

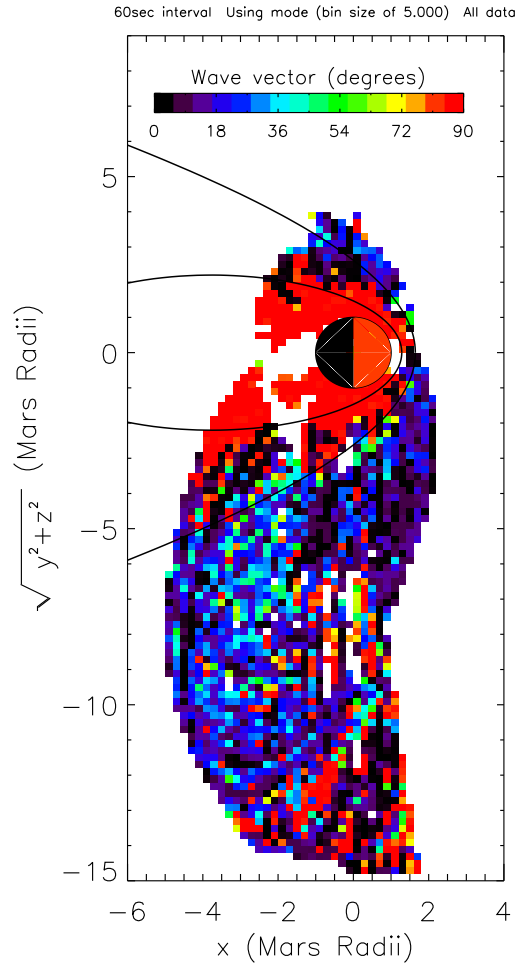


Figure 4.16: The wave vector (angle of propagation) relative to the mean field for the predominant wave form of the interval. Only intervals that have ratios of 3 or greater for the MVA intermediate and minimum eigenvalues are counted.

available and surely much interesting science awaits to be discovered in them. Many of these other intervals will also illustrate properties that are not compatible with the statistical properties just described. This is to be expected given the large variations in solar cycle averaged over in the statistical results. The intervals here were specifically chosen to demonstrate some of the statistical results and I leave the analysis of many of the other individual orbits for future work (though see chapters 5 and 6).

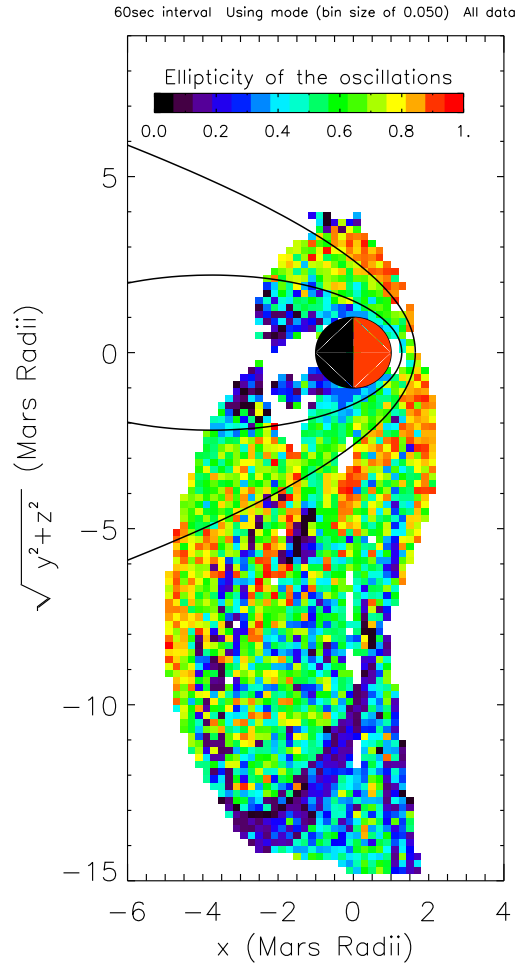


Figure 4.17: The ellipticity of the components in the directions of maximum and intermediate variance. An ellipticity of 1 represents perfectly circular polarization whereas an ellipticity of 0 represents perfectly linear polarization.

4.2.1 *m98d101*

The first case study I include is from 11 April, 1998 (or decimal day 101). The interval chosen is from the dayside magnetosheath and starts around decimal day 101.192 and lasts for 300 seconds. The top two panels of figure 4.22 show the $|B|$ and 191 eV electron flux for the entire pass with the selected interval indicated by dotted lines. It is clear that our interval starts at the MPB, which is clearly discernible

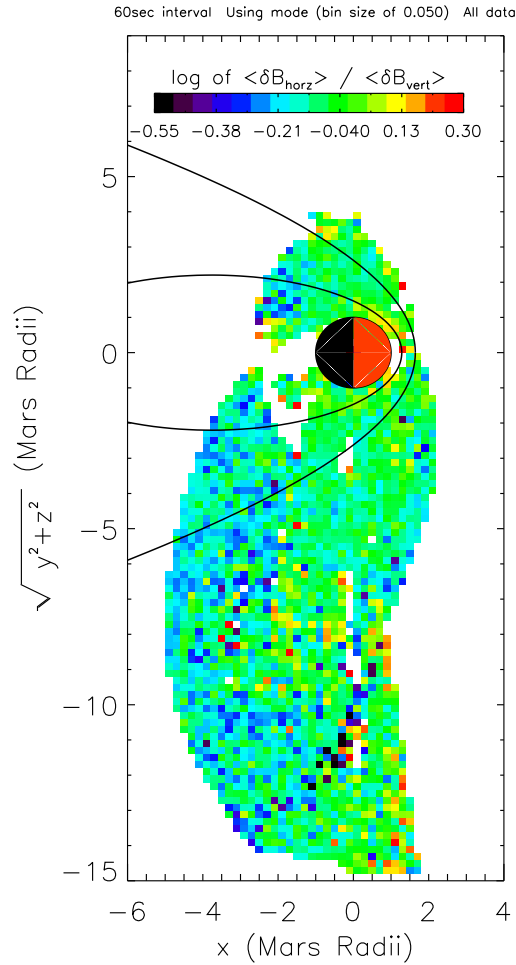


Figure 4.18: The ratios of the tangential (horizontal relative to the planetary surface) and radial (vertical) amplitudes for the 60 second intervals.

by the sharp increase in $|B|$ and the sharp decrease in the electron flux. The three panels below show, respectively, the B_{\parallel} , B_{\perp} , and relative electron flux fluctuations. The oscillations of interest are clearly evident in all three components. The upper right panel shows the location of MGS during the interval and the bottom right panel shows a hodogram of the magnetic field fluctuations in the directions of maximum and intermediate variance.

Figures 4.23 and 4.24 show wavelet analyses for the B_{\parallel} and B_{\perp} fluctuations for

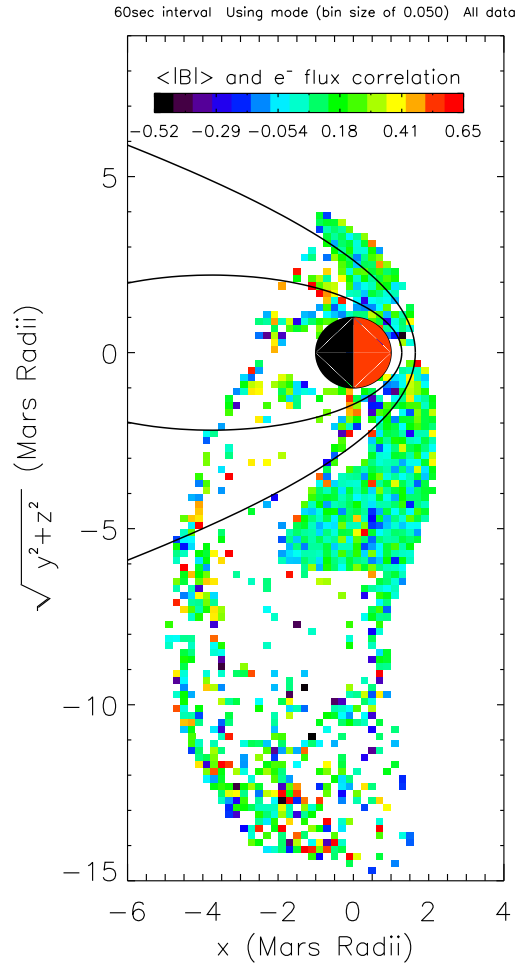


Figure 4.19: The correlation coefficient between the 191 eV electron flux and the $|B|$ data for the 60 second intervals. A coefficient of 1 represents a perfect correlation, a coefficient of 0 represents no correlation at all, and a coefficient of -1 represents a perfect anti-correlation.

the interval. The left hand panels show the wavelet power spectra and the right hand panels show the global (time integrated) spectra. Superimposed are lines indicating the local proton, helium, and oxygen gyrofrequencies. The B_{\parallel} fluctuations show broad spectral power from 0.01 Hz to around 0.2 Hz (just below the proton gyrofrequency). The B_{\perp} fluctuations show spectral power in two main peaks at ≈ 0.1 Hz (between the proton and helium gyrofrequencies) and at ≈ 0.02 Hz (nearly exactly at the oxygen gyrofrequency).

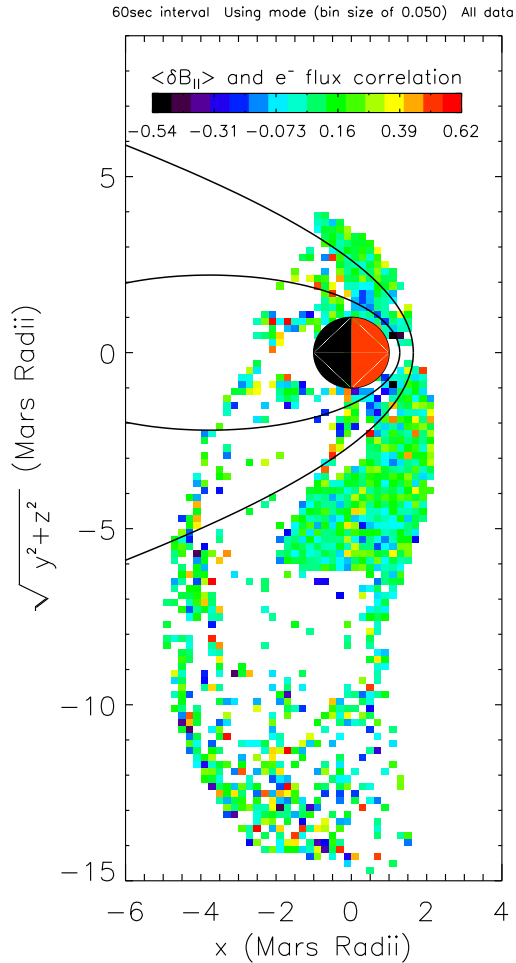


Figure 4.20: The correlation coefficient between the 191 eV electron flux and the $B_{||}$ data for the 60 second intervals. A coefficient of 1 represents a perfect correlation, a coefficient of 0 represents no correlation at all, and a coefficient of -1 represents a perfect anti-correlation.

Table 4.1 shows some of the measured wave properties of the fluctuations in the interval. The waves are compressional at all frequencies, and especially in the 0.01 to 0.1 Hz range. They are linear in amplitude, have a wave vector nearly perpendicular to the mean magnetic field, and are more circularly than linearly polarized. They show fairly strong correlations with the electron flux fluctuations and have larger amplitudes in the direction tangential to the planetary surface than in the direction radially away from the planet. Combined with the spectral analyses, these results

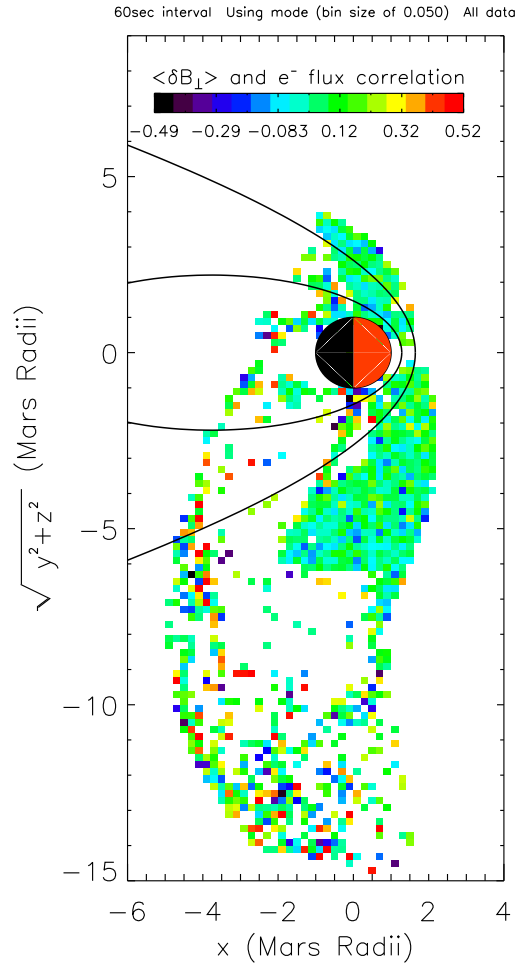


Figure 4.21: The correlation coefficient between the 191 eV electron flux and the B_{\perp} data for the 60 second intervals. A coefficient of 1 represents a perfect correlation, a coefficient of 0 represents no correlation at all, and a coefficient of -1 represents a perfect anti-correlation.

present a complicated picture. Nonetheless, generally speaking, these properties are the same ones that we observed to be the most likely to be present in the dayside magnetosheath and MPR.

4.2.2 *m98d152*

The second interval that I have chosen as an example is from 1 June 1998 (or decimal day 152). The interval starts around decimal day 152.58, lasts for 600 seconds,

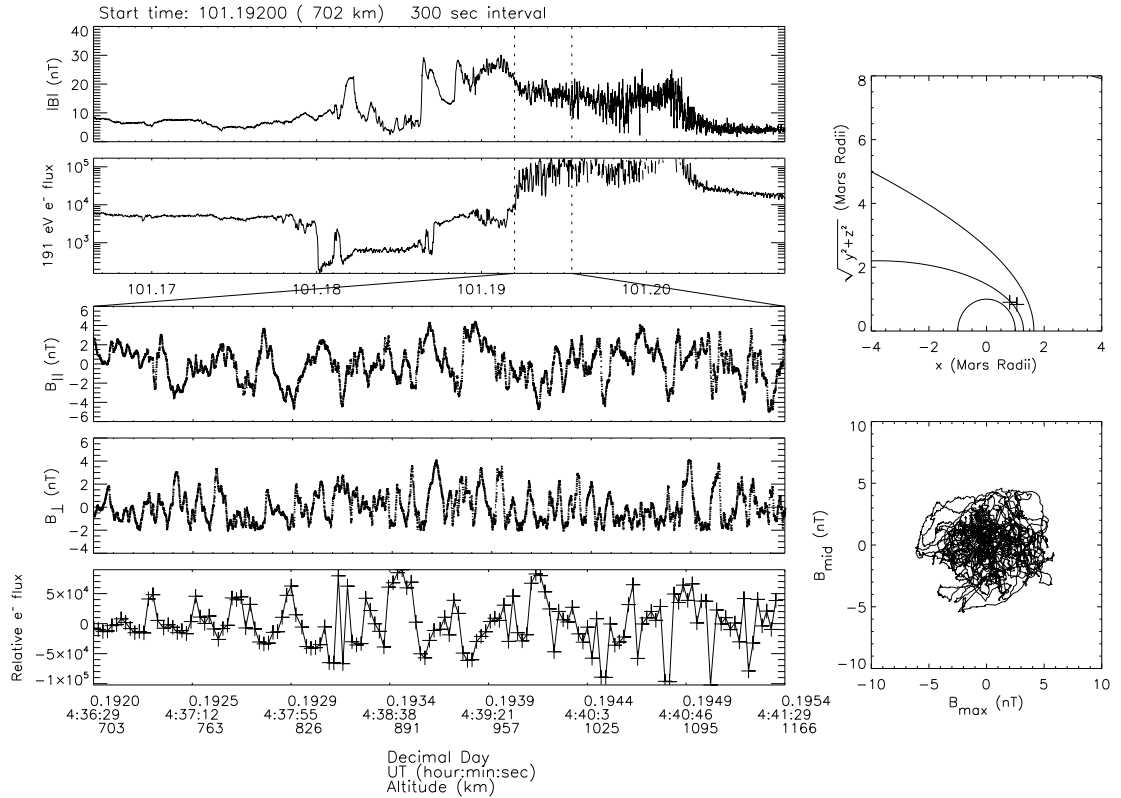


Figure 4.22: Oscillations from a 300 second interval during 11 April, 1998 (decimal day 101). The top two panels show the magnetic field magnitude and 191 eV electron flux for the entire pass whereas the bottom three panels show, respectively, the parallel, perpendicular, and the relative electron flux fluctuations for the selected interval. The upper right panel shows the MGS location during the interval marked as a plus sign and the lower right panel shows the magnetic field components in the directions of the maximum and intermediate eigenvalues of the variance.

and is in the nightside magnetosheath. Figures 4.25, 4.26, and 4.27 show (in the same manner as figures 4.22, 4.23, and 4.24 do for the previous interval) the time series data and the wavelet analyses for the interval. Table 4.1 also lists the quantitative results for the analysis of the waves.

The numerical data paint a picture of waves that are predominantly transverse at higher frequencies and predominantly compressional at lower frequencies; that

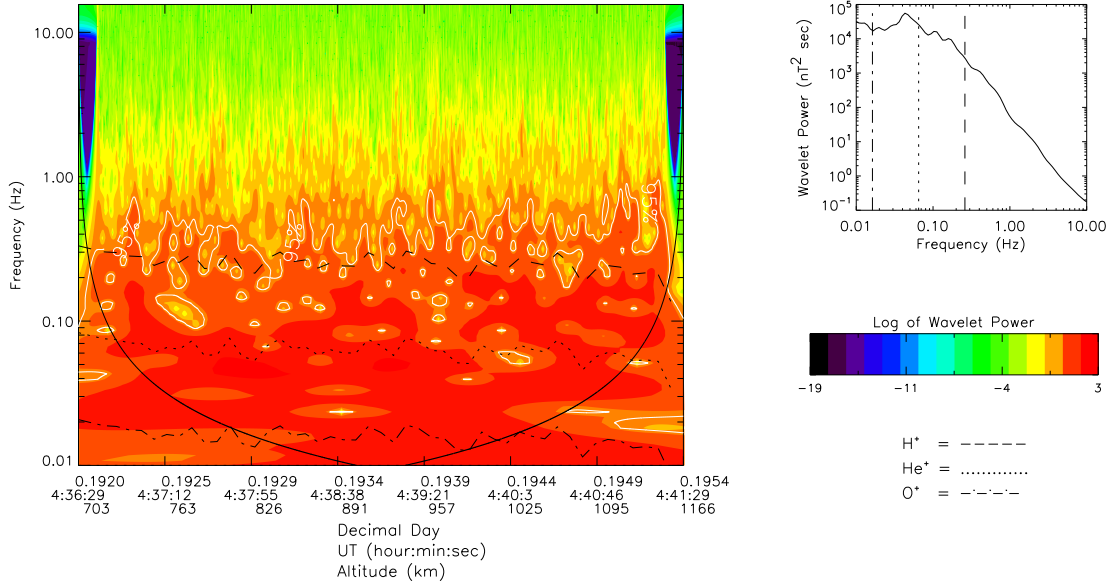


Figure 4.23: The wavelet spectral analysis of the B_{\parallel} component for the interval shown in figure 4.22. The left panel shows the wavelet power spectrum while the right panel shows the global wavelet power spectrum. The dashed lines indicate the average hydrogen gyrofrequency, the dotted lines the helium gyrofrequency, and the dashed-dotted lines the oxygen gyrofrequency.

are elliptically polarized and have a left hand sense of polarization; that they exhibit correlations between the ER and MAG data (except for the B_{\perp} data); and that they have larger amplitudes in the radial direction than in the tangential direction. Figure 4.26 shows that most of the spectral power in the B_{\parallel} component is present at the lowest observed frequencies (between 0.01 and 0.02 Hz), although a local spectral peak exists right above the local proton gyrofrequency at 0.3 Hz. Figure 4.27 shows the B_{\perp} spectral power distributed in a series of peaks at 0.2 Hz (right at the proton

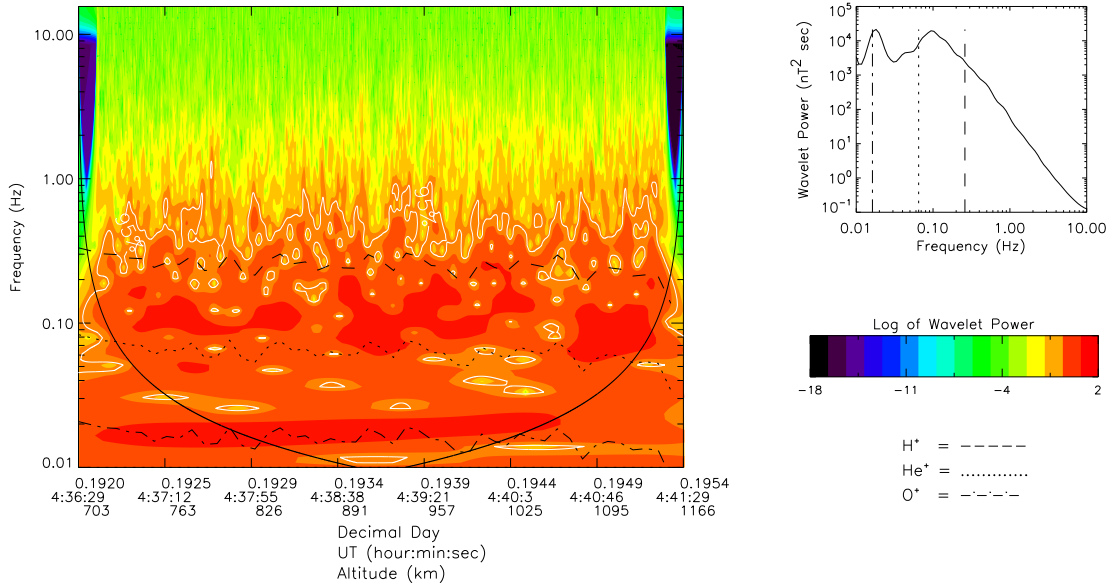


Figure 4.24: The same as figure 4.23 except for the B_{\perp} component.

gyrofrequency), around 0.08 Hz, at 0.02 Hz, and at 0.01 Hz (just below the oxygen gyrofrequency). Again, a complex mix of wave modes appears to be present, but in general, all of these properties are similar to the general statistically likely properties identified in the previous section. Therefore, I identify this interval as a typical interval for the nightside magnetosheath.

4.2.3 *m98d209*

The last example I include is from 28 July 1998 (decimal day 209). The solar wind magnetic field was much higher (~ 20 nT) than normal during this orbit and

Table 4.1. Wave properties of case examples

Property	Example 1	Example 2	Example 3
Start time (decimal day)	101.192	152.583	209.88
Interval length (secs)	300	600	60
$ B $ (nT)	17.1	14.5	33.9
$\delta B/ B $	0.12	0.09	0.13
$\log_{10} \delta B_{ }/\delta B_{\perp}$	0.110	-0.105	0.023
$\log_{10} \delta B_{ }/\delta B_{\perp}$ for 1 to 10 Hz	0.093	-0.458	0.965
$\log_{10} \delta B_{ }/\delta B_{\perp}$ for 0.1 to 1 Hz	0.020	-0.642	2.42
$\log_{10} \delta B_{ }/\delta B_{\perp}$ for 0.01 to 0.1 Hz	0.508	0.408	1.45
$\log_{10} \delta B_{ }/\delta B_{\perp}$ for 0.001 to 0.01 Hz	0.152	0.375	N/A
Wave vector (degrees)	85.2	N/A	N/A
Ellipticity	0.739	0.460	0.365
Relative sense of polarization	0.043	-0.260	-0.48
$\log_{10} \delta B_{horz}/\delta B_{vert}$	0.205	-0.059	-0.032
Correlation $ B $ and electron flux	-0.369	0.459	0.14
Correlation $B_{ }$ and electron flux	-0.290	0.326	0.10
Correlation B_{\perp} and electron flux	-0.195	-0.162	-0.22

the fluctuations are enhanced during the interval. The chosen interval occurs near the day-night terminator within the magnetosheath and lasts for 60 seconds. As with the previous examples, Table 4.1 lists the quantitative measures of the wave characteristics. Figure 4.28 shows the time series in the same form as the previous examples with one exception; the bottom panel shows θ , the angle of rotation of the perpendicular components around the mean field. The fact that the slopes of the lines are mostly negative indicates that this interval is marked by largely left handed (clockwise) polarization. Figures 4.29 and 4.30 show the wavelet analyses for the interval.

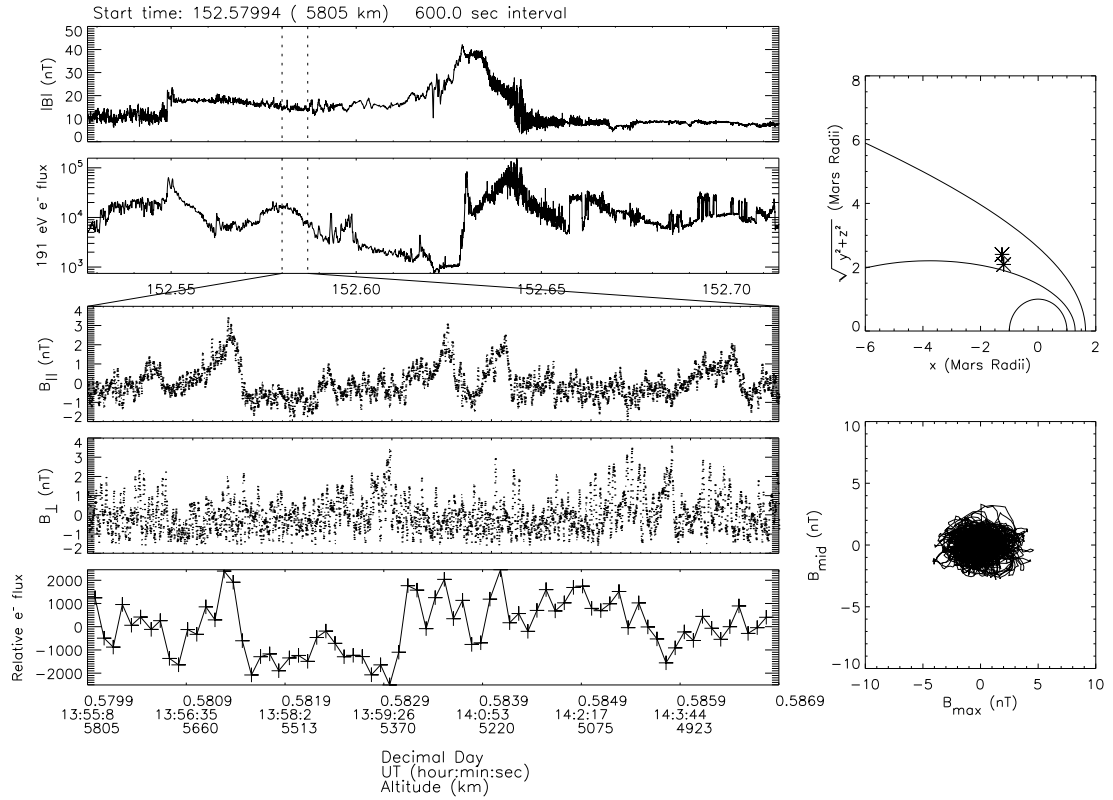


Figure 4.25: The same as figure 4.22 except for an interval in the nightside magnetosheath during 1 June 1998 (decimal day 152).

These figures and the quantitative data indicate that this interval has large, coherent, left hand elliptically polarized waves with significant spectral power within a factor of 2-3 of the proton gyrofrequency and predominant power in the B_{\parallel} component. This interval shows some of the characteristics found in the statistical results but also shows distinct features. The regularity of the left handed polarization is particularly striking during this interval.

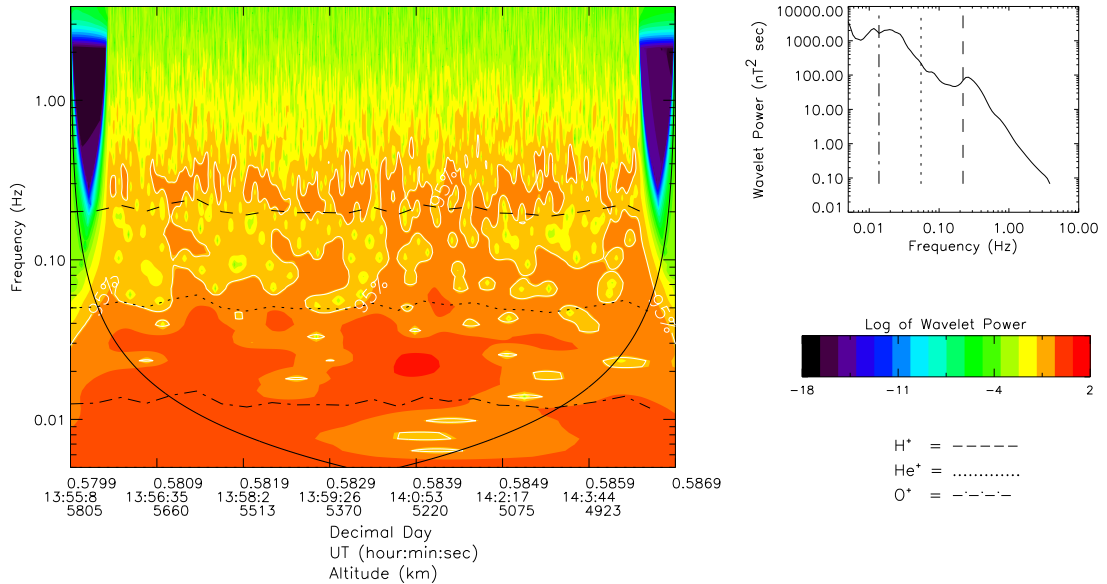


Figure 4.26: The B_{\parallel} component for the interval of figure 4.25.

4.3 Discussion of results

Can we make sense of the foregoing observations and derive some physical information from them? Certainly, it is the case that the near Mars space is a complex plasma environment. The solar wind contains its own perturbations which propagate through the region as the solar wind interacts with the Martian ionosphere. Fluctuations produced at the bow shock may propagate downstream of the shock or upstream depending on the plasma speed and the wave speed. Fluctuations in the ionospheric plasma interact with the fluctuations convected down from the solar wind. All the while, the planet rotates underneath, bringing the crustal fields and their associated

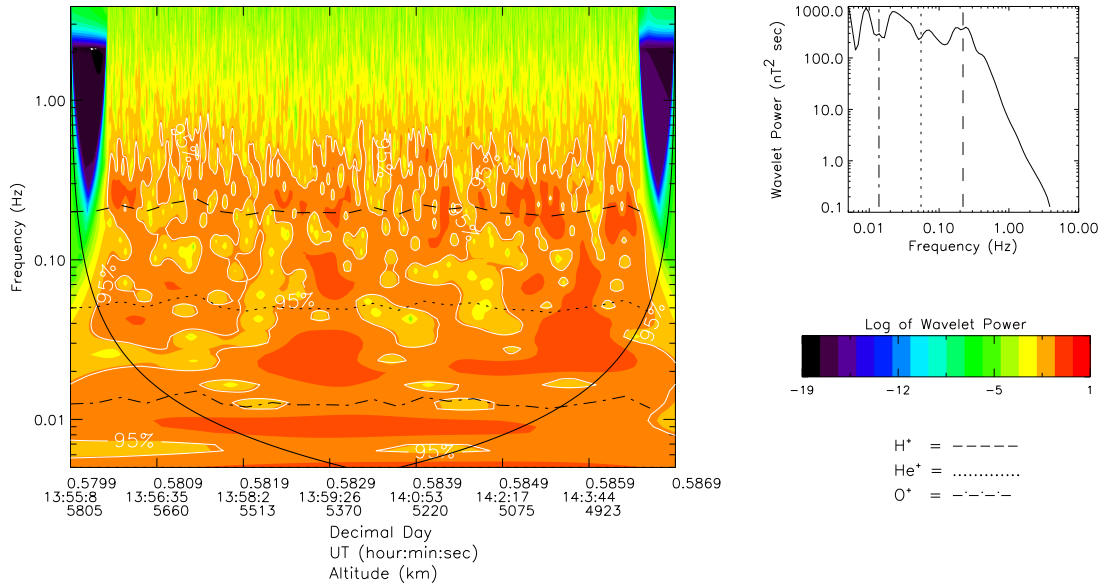


Figure 4.27: The B_{\perp} for the interval of figure 4.25.

mini-magnetospheres in and out of contact with the upper regions of the interaction. Furthermore, there are several populations in the plasmas that interacting; there are hot protons from the solar wind, small amounts of heavy ions in the solar wind, large quantities of relatively cool protons and O^+ ions planetary origin, and the associated electron populations. Hence we can expect waves and instabilities associated with each of these populations and with the interactions of these populations.

Despite these complications, I believe it is possible to make some headway in interpreting the observations presented here. Currently, more instrumentation would be welcome (ion spectrometers on a spacecraft with a magnetometer would be most

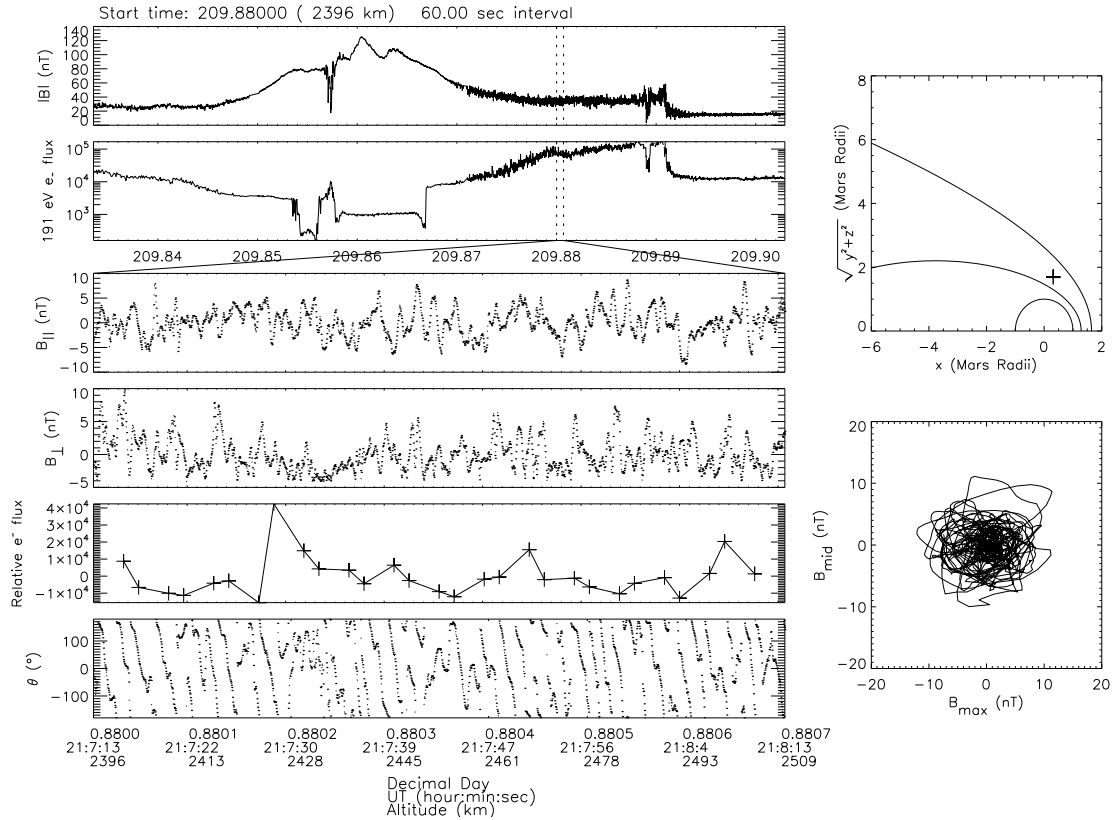


Figure 4.28: A figure similar to figure 4.22 for an interval near the terminator in the magnetosheath during 28 July 1998 (decimal day 209). Here I plot, in the bottom panel, the rotation angle (θ) of the perpendicular component.

welcome) as would multiple spacecraft flying in formation (e.g. the Cluster spacecraft at Earth). Ground based observations would also be of great benefit, especially since observers have literally centuries of experience with ground based observations of low frequency fluctuations at Earth. Nonetheless, using the MGS observations presented here we can make a beginning in understanding the low frequency plasma waves present at Mars.

One of the first things that we can do is to look at what sorts of theoretical wave modes might be expected. The information about theoretical wave modes can

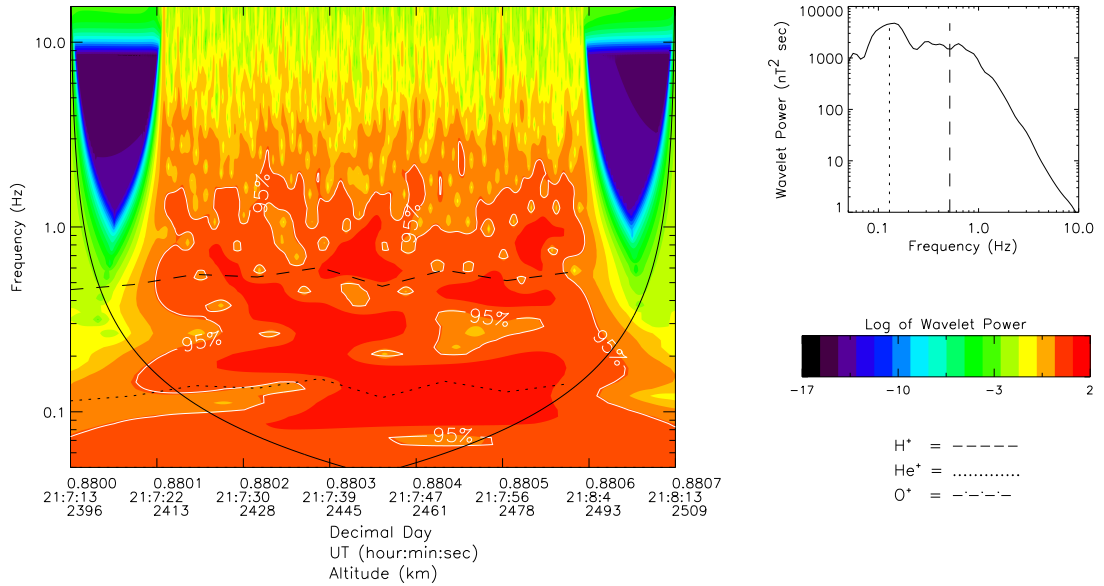


Figure 4.29: The B_{\parallel} wavelet analysis for the interval of figure 4.28.

be utilized in two ways: one, we can look at the types of wave modes that the observations indicate to be present and hence deduce the physical conditions present; two, we can use the physical conditions likely to be present to deduce the types of waves mode likely to be present and we can look for characteristics of these waves in the observations.

In order to discuss theoretical wave modes, I need to decide where in several important parameter regimes the observed wave modes are most likely to fall. Generally speaking, two main approaches have been taken to describing plasma waves; either magnetohydrodynamic theories (MHD) that treat the plasma as a fluid or plasma

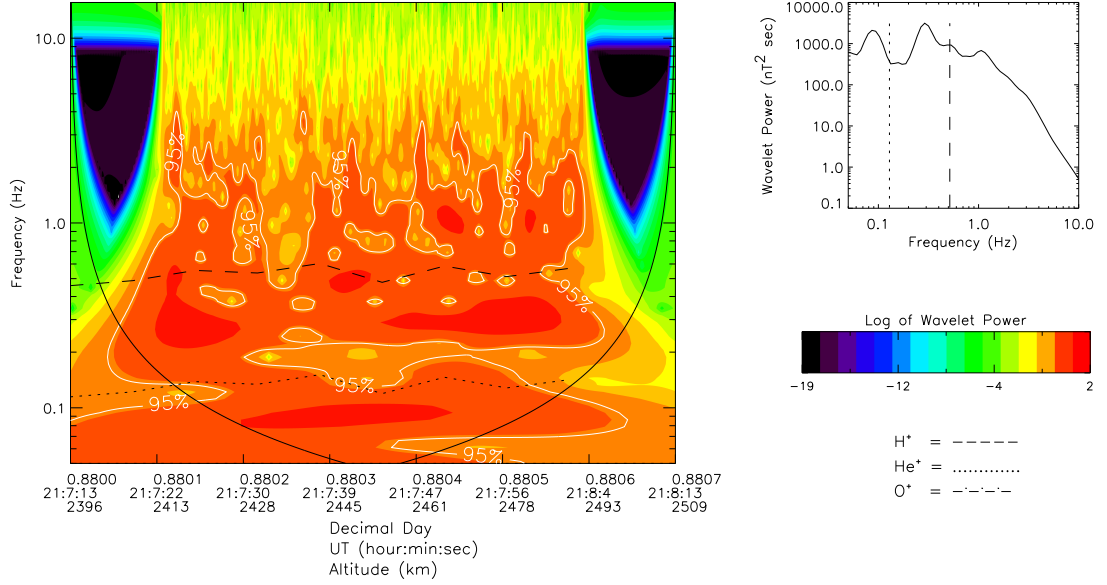


Figure 4.30: The B_{\perp} wavelet analysis for the interval of figure 4.28.

kinetic theories based on the Vlasov equation. Fluid based theories yield three well known wave modes often known as the fast, intermediate, and slow modes in reference to their relative phase speeds. This fluid description, although conceptually simpler and more widely familiar, has been shown to be unlikely to be accurate for high β plasmas (where β , the ratio of particle pressure to magnetic pressure) such as planetary and cometary magnetosheaths [Orlowski *et al.*, 1994; Krauss-Varban *et al.*, 1994]. β is defined as

$$\beta = \frac{nk_B T}{B^2/2\mu_0} \quad (4.1)$$

with n being the number density of the plasma, T its temperature, μ_o the permeability of free space, and k_B is the Boltzmann's constant.

Quantitative verification that the Martian magnetosheath is a high β regime is difficult because the available measurements of the ion temperature in the magnetosheath vary by as much as an order of magnitude (cf. figure 6.8 of *Nagy et al.* [2004]). However, by analogy with other magnetosheaths and by noting the basic plasma physics principle that temperatures increase in postshock regions, I find it very plausible that the Martian magnetosheath will be a relatively high β (> 1) region. On the other hand, the MPR and the ionosphere should be regions of relatively low β as the magnetic field magnitude increases but the plasma temperature becomes much cooler as planetary ions come to dominate the population. Thus within the magnetosheath, I expect the wave modes present to be those that exist in relatively high β conditions and I also expect that kinetic plasma theory will do a better job describing these waves.

The simplest kinetic based theories assume homogeneous isotropic plasma distributions and also yield three wave modes though these modes do not correspond directly to the three MHD modes. More complicated kinetic descriptions include plasma temperature anisotropies and non-Maxwellian distribution functions (such as beams of plasma streaming past each other). Each of these complications produces changes in the possible wave modes. Most of the work done on this subject has used linear Vlasov theory because linearizing the equation makes the analytic mathemat-

ical treatment tractable. Unfortunately, for many of the fluctuations observed in the Martian magnetosheath (especially for the 600 second intervals) $\delta B/|B| > 0.25$ and so linear theory is unlikely to be always applicable. A fully developed nonlinear kinetic wave mode theory appears to have not yet been developed.

Nonetheless, given that the fluctuations are not always fully nonlinear, I consider several of the theoretical wave modes to see if they fit the observations. *Gary* [1992], *Gary* [1993], and *Gary et al.* [1993] found that several low frequency plasma instabilities grow for anisotropic proton-electron plasmas. In particular, when the plasma temperature perpendicular to the background field (T_{\perp}) is greater than the plasma pressure parallel to the field (T_{\parallel}) then two main modes develop – the mirror instability and the proton cyclotron anisotropy instability. These two instabilities grow in competition with each other whenever their anisotropy conditions are met, with the proton cyclotron instability growing faster than the mirror mode for a homogeneous plasma of $\beta < 6$ (as is expected in the Martian magnetosheath). However, the addition of a relatively small density of heavier ions causes the growth rate of the proton cyclotron instability to be significantly decreased and thereby allows the mirror instability to become the dominant mode in an anisotropic plasma [*Price et al.*, 1986]. Such a situation occurs in the Martian magnetosheath since the relatively large exosphere has been calculated to extend out to magnetosheath altitudes [e.g. *Chen and Cloutier*, 2003].

Mirror mode oscillations have their largest growth rate for wave vectors perpen-

dicular to the background magnetic field, have very low real frequencies in the plasma frame (and hence very low frequencies in the frame of a relatively slow moving observer), are more compressional than transverse, have anti-correlations between the plasma and field fluctuations, and are generally linearly polarized. All these properties match the observed properties of many of the fluctuations in the dayside magnetosheath so I suggest that these fluctuations are mirror mode oscillations. It is important to remember, however, that the theory used in this determination is a linear theory and that many of the oscillations observed are in the nonlinear regime.

Besides the fact that the observed properties match those of the mirror mode, is there any reason to expect the mirror mode in the dayside magnetosheath? Identifications of mirror mode waves have been made in similar physical environments, such as the terrestrial magnetosheath [e.g. *Schwartz et al.*, 1996 and references therein] and near the MPB of comets [*Mazelle et al.*, 1991; *Glassmeier et al.*, 1993]. In these other environments, plasma depletion layers [*Crooker and Siscoe*, 1977] have been identified that give rise to the temperature anisotropies necessary for the mirror mode to develop. Such a plasma depletion layer has been recently discovered near the MPB at Mars [*Oieroset et al.*, 2004]. The identification of mirror mode waves in the magnetosheath reinforces this discovery of a plasma depletion layer at Mars. This conclusion is similar to one reached by *Bertucci et al.* [2004].

I turn now to a discussion of theory that may be applicable to the fluctuations in the nightside magnetosheath. Besides describing instabilities due to plasma

anisotropies, kinetic theories also give results for fluctuations due to non-Maxwellian plasma distributions (e.g. beams of plasma streaming past each other or interacting with cores or rings of different plasma populations). *Gary* [1991; 1993] gives a good summary of results from kinetic theory for various configurations of interacting plasmas. He finds that for an ion core drifting relative to a less dense ion beam that several low frequency modes are unstable – the ion/ion right-hand resonant instability, the ion/ion left-hand resonant instability, and the ion/ion nonresonant instability. All three of these instabilities have their largest growth rates for propagation parallel to the background field but the nonresonant instability only has significant growth when the relative drift speed between the components is significantly higher than the Alfvén speed. This is not expected to be the case downstream of the Martian shock so I consider only the resonant instabilities. The senses of polarization for these instabilities are given in the plasma frame and the Doppler shift to the measurement frame sometimes switches the sense of polarization (especially in the case that the waves propagate upstream against the plasma bulk velocity [*Thorne and Tsurutani, 1997*]). Therefore, I neglect the sense of polarization when considering these modes and refer to both modes simply as ion/ion resonant instabilities.

The ion/ion resonant instabilities give rise to transverse fluctuations that have their largest growth rates when propagating along the mean magnetic field. They also show correlations between the plasma and field perturbations and typically have frequencies, in the frame of the plasma, within an order of magnitude of the local ion

gyrofrequency. These characteristics match those of many of the fluctuations observed in the nightside magnetosheath and hence I suggest that many of those fluctuations are in fact ion/ion resonant instabilities. The solar wind sees the planetary ions as a beam of relatively cold ions and as these two plasmas sweep past each other, the resonant ion/ion instabilities set in and the planetary ions are picked up and carried away by the solar wind's magnetic field.

An alternative to the kinetic description provided in the foregoing is the theory of oscillitons. In a recent article *Dubinin et al.* [2003] provide the current version of this theory. They solve the fully nonlinear Hall-MHD equations for a warm proton-heavy ion plasma. They find instabilities that develop as a result of the Lorentz force acting between the proton and heavy components as they inertially drag each other back and forth. In *Dubinin et al.* [2004] certain of these solutions develop both stationary structures (solitons) and oscillatory structures; hence the name oscillitons. These oscillitons are packets of gyrating ions embedded in an overall semi-stationary wave packet. They propagate parallel to background field and the oscillatory part of their signature has plasma frame frequencies near both the proton and heavy ion gyrofrequencies. They assert that such theory may be useful in explaining waves found at both Mars and comets where such nonlinear, two-component waves are commonly found. However, they also acknowledge the difficulties in using fluid theory for relatively high β plasmas such as the Martian magnetosheath. However, they argue that, because the proton and oxygen gyroradii in the near Mars space are

comparable to the size of the interaction region, then finite gyroradius effects (one of the main advantages of kinetic theories) are not so important in the Martian case. They also emphasize that their framework has the advantage of being fully nonlinear whereas they point out the difficulties in solving the nonlinear Vlasov equation. It is the case that the described wave characteristics of their oscillitons match many of the characteristics observed in the nightside magnetosheath; waves with frequencies near the ion gyrofrequencies are observed there, they do often propagate parallel to the mean magnetic field, and higher frequency components are observed to be embedded in larger, lower frequency structures.

In any case, from a simplistic point of view, both of these frameworks are telling us the same picture. The H^+ and O^+ ions produced from the planetary ionosphere create a highly anisotropic distribution as they are picked up by the solar wind's magnetic field. As the plasma attempts to return to isotropy, this distribution drives electromagnetic ion cyclotron waves unstable with resonances near their gyrofrequencies. We observe these ion cyclotron waves as they propagate through the magnetosheath and into interplanetary space.

I note in closing one last simple physical interpretation, which is suggested by the observed radial and tangential amplitudes (figures 4.10 and 4.18). Since the commonly observed frequencies in the dayside magnetosheath are as low as 0.01 Hz (cf. figure 4.23) and the typical post-shock Alfvén speed is about 100 km/s [*Nagy et al.*, 2004], we can estimate that wavelengths as large as 1600 km are typical there. This is nearly all

the way across the magnetosheath for most dayside SZAs and suggests an explanation for the larger tangential amplitudes there. Waves that happen to be oriented radially to the planetary surface are selectively damped since, with their large wavelengths, they sample the lower portions of the MPR. Wave that are oriented tangentially are able to complete their full cycle without encountering increased densities. It is possible this mechanism contributes to production of the temperature anisotropies mentioned in regards to the mirror mode waves.

Chapter 5

Results during the October 2003 solar storm

In this section I report on the low frequency plasma waves produced during the large solar storms of October 2003. Most of the text in this section taken from *Espley et al.* [2005a] with minor editing for inclusion in this thesis.

5.1 Introduction

The 2003 October-November solar storms produced a variety of phenomena across the solar system. *Cridder et al.* [2005] use observations from Mars Global Surveyor (MGS) to show that the plasma interaction region at Mars is compressed during the passage of the coronal mass ejection (CME) that was launched from the Sun on October 28, 2003. In this work, we focus our attention on MGS observations (at an altitude of 400 km) of changes in the magnetic oscillations observed at Mars. In particular we find that a wide variety of oscillations occur in the normally tranquil magnetotail and that, in some instances, the character of the oscillations in the dayside magnetic pileup region (MPR) changes during the passage of the storm.

Espley et al. [2004] used MGS observations to characterize the general character of low frequency oscillations in the near Mars space. They determined that the dayside magnetosheath is dominated by mirror mode waves, that the nightside magnetosheath is dominated by resonance cyclotron waves created by the interaction of the solar wind plasma with plasma of planetary origin, and that the nightside MPR and tail region contain relatively little oscillatory activity. We compare this general picture to the dramatic changes observed during the passage of the solar storm.

MGS arrived at Mars in 1997 and since that time the Magnetometer/Electron Reflectometer (MAG/ER) investigation has been returning a steady flow of data [*Acuña et al.*, 2001]. When MGS first arrived at Mars it began a slow process of aerobraking in order to circularize its orbit. During these “pre-mapping” phases of the mission, MGS sampled a large variety of altitudes and solar zenith angles (SZAs) as its elliptical orbit was gradually brought down to the circular mapping orbit which it reached in February of 1999 [*Albee et al.*, 2001]. All data returned since that time have been from the near circular mapping orbit which has an approximate altitude of 400 km, an orbital period of 2 hours, and covers 0200 to 1400 in local time. Hence the data we use in this study are confined to this narrow altitude range unlike the study of *Espley et al.* [2004] which was able to use pre-mapping data to cover large spatial regions.

5.2 Observations

In order to illustrate the oscillations observed during the passage of the solar storm, we select a number of intervals to analyze in depth. Figure 5.1 shows the first interval chosen, decimal day 303.402 to 303.405. In top left panel, the magnetic field magnitude ($|B|$) for the entire day of October 30, 2003 (decimal day 303) is shown versus time. MGS's passage from the day side (when $|B|$ is high) to the night side (when $|B|$ is low) is clearly seen as MGS makes approximately 12 orbits during that day. The main shock wave from the solar storm seems to have hit around 303.2 when $|B|$ increases to well above its normal levels ($|B|$ is normally about 30 nT on the night side and near 60 nT on the day side at these altitudes). The panels below the $|B|$ profile show the MF magnetic field components for the region of interest. The last panel on the left shows the relative omni-directional flux ($cm^{-2}s^{-1}sr^{-1}eV^{-1}$) of electrons with energies of 191 eV. In the upper right, we show as plus signs the starting and ending locations (which overlap on this scale) of MGS for the interval in SS coordinates. We also show the best fit locations of the bow shock and MPB from *Vignes et al.* [1999]. In the lower right panel, we show the perpendicular components of the magnetic field in MF coordinates plotted versus each other (a hodogram). Figures 5.2 and 5.3 show wavelet transforms of approximately the same interval for the $B_{||}$ and B_{\perp} components respectively. The left panels show the wavelet power spectra whereas the right panels show the global (time integrated) wavelet power spectra. The dashed line indicates the average hydrogen gyrofrequency, the dotted

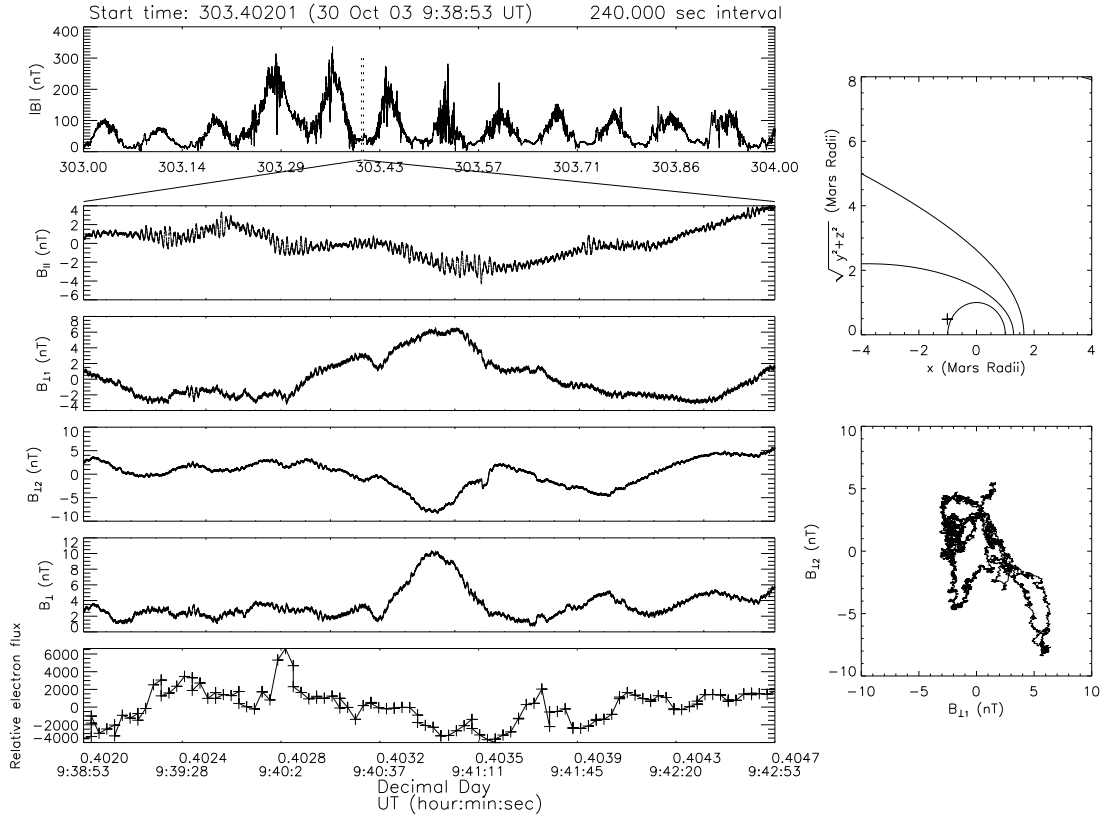


Figure 5.1: A detailed analysis of the interval from decimal day 303.402 to 303.405 (October 30, 2003). (Top left) The $|B|$ time profile for the entire day with dashed lines indicating the interval of interest analyzed below. (Left panels from 2nd to top to bottom) These panels show the $B_{||}$, $B_{\perp 1}$, $B_{\perp 2}$, B_{\perp} , and relative electron flux for the interval of interest. (Top right) The starting and stopping locations of MGS (shown as +) during the interval analyzed in SS coordinates. Also shown are the best fit bow shock and MPB curves. (Bottom right) The hodogram of the B_{\perp} components for the interval.

line the helium gyrofrequency, and the dashed-dotted line the oxygen gyrofrequency.

During non-storm periods at this location, far on the night side at approximately 400 km, the magnetic field is weak and coherent oscillations are almost undetectable (see the third case example). However, in this case (about 5 hours after the main shock wave seems to have hit Mars), the field is relatively high (38 nT) and there is clear spectral power at a variety of frequencies. Most striking is the clear signal at the local

hydrogen gyrofrequency (about 0.6 Hz) in the B_{\parallel} oscillations. This signal is clearly evident in the B_{\parallel} time series. Spectral power at this frequency is also seen in the B_{\perp} component although it is considerably weaker. Interestingly, there is also spectral power in both components at frequencies lower than the oxygen gyrofrequency (0.04 Hz). This lower frequency signal exhibits more spectral power in the B_{\perp} component and is evident in a qualitative inspection of that component. It should be noted that these observed frequencies are in the frame of the moving spacecraft. However, since the average velocity of MGS in the mapping orbit is about 4 km/s, it is expected that the Doppler shift from the spacecraft frame to plasma frame should be small.

The hodogram shows that the perpendicular components are quite variable during the interval although there are periods when they are fairly linearly polarized. The overall ellipticity during the interval is 0.4. Using MVA, the ratio of the intermediate to minimum eigenvalues is 2.5 which when combined with the periods of linear polarization during the interval makes somewhat uncertain the calculated direction of propagation (19° relative to the mean field) for the dominant wave mode. The relative sense of polarization for the interval is -0.02 meaning that the perpendicular components are neither predominately left-handed nor right-handed polarized but are rather a fairly even mix. The correlation coefficient between the relative 191 eV electron flux and the B_{\parallel} component is 0.47 and between the electron flux and the B_{\perp} component the coefficient is -0.10.

Figures 5.4, 5.5, and 5.6 show plots similar to figures 5.1, 5.2, and 5.3 for another

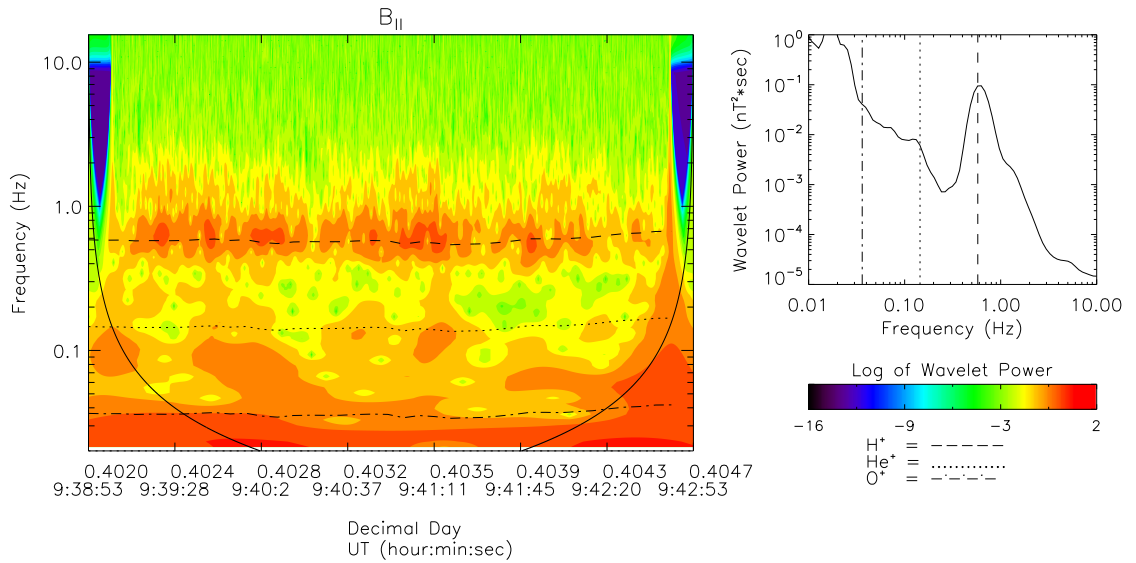


Figure 5.2: The wavelet spectral analysis of the B_{\parallel} component for the interval shown in figure 5.1. The left panel shows the wavelet power spectrum while the right panel show the global wavelet power spectrum. The dashed lines indicates the average hydrogen gyrofrequency, the dotted lines the helium gyrofrequency, and the dashed-dotted lines the oxygen gyrofrequency.

illustrative interval - decimal day 303.233 to 303.2413. MGS was on the night side during this interval also. However, this interval is near the time when the main shock from the solar storm was hitting Mars. The mean $|B|$ for the interval is 55 nT, the mean relative polarization is 0.01, the intermediate to minimum MVA eigenvalue ratio is 1.7 (rendering unreliable the calculated 68° propagation angle relative to the mean field), and the total ellipticity is 0.84 (as seen by the roundness of the hodogram). The correlation coefficients between the relative electron flux and the B_{\parallel} and B_{\perp}

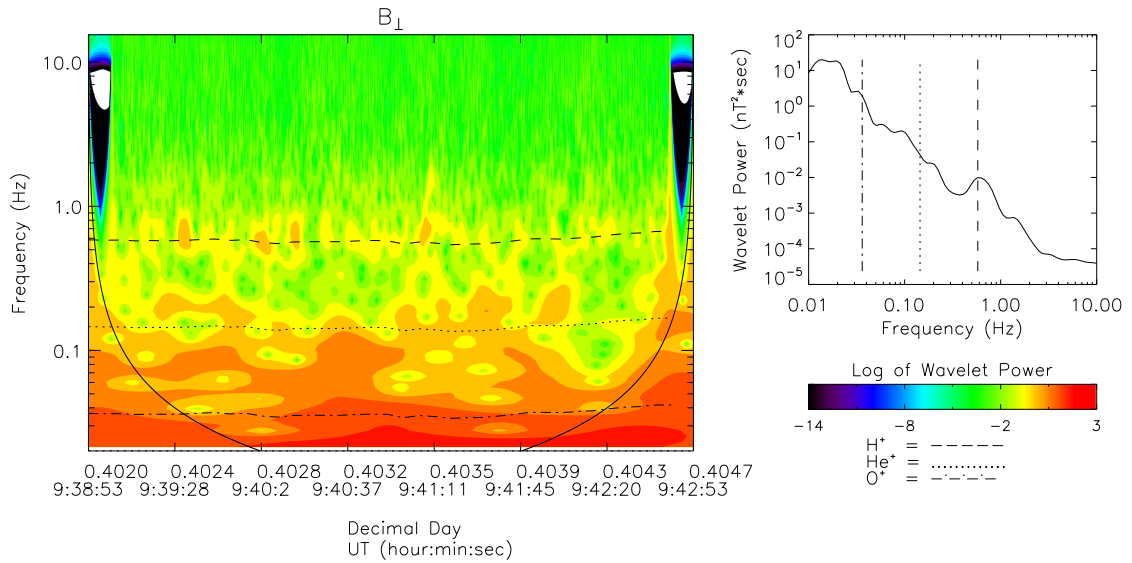


Figure 5.3: The same as figure 5.2 except for the B_{\perp} component.

components are 0.32 and -0.24 respectively.

Qualitative inspection of the time series of the magnetic components reveals considerable oscillatory activity at a variety of frequencies. The wavelet power spectra in figures 5.5 and 5.6 confirm this picture. More power at a wider range of frequencies is displayed in the B_{\parallel} component although the B_{\perp} component also has considerable power. In both cases, the greatest spectral power is displayed at frequencies at and below the local oxygen gyrofrequency.

To provide contrast with the phenomena observed in the previous two case studies, figure 5.7 shows a plot similar to figure 2 for an interval from a day (September 7, 2003

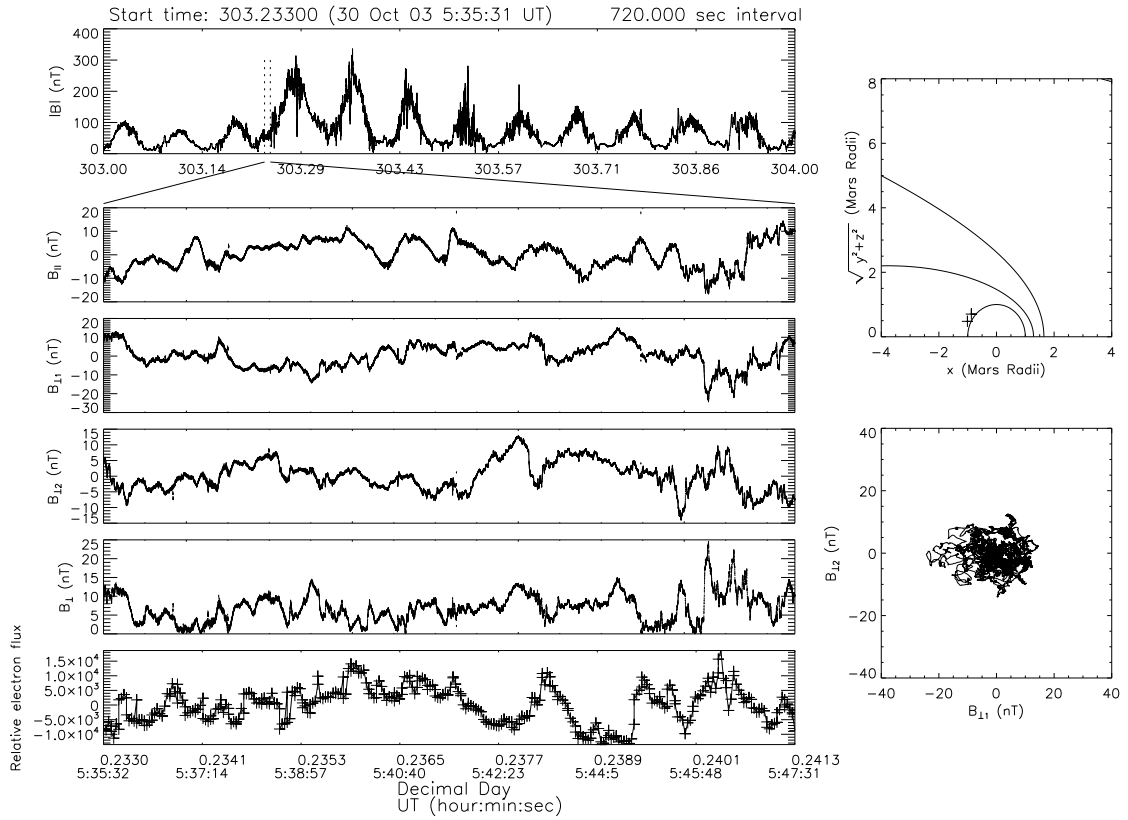


Figure 5.4: The same as figure 5.1 but for interval of 303.233 to 303.2413.

or decimal day 250) showing little evidence of unusual solar activity. On September 5, 2003, according to data publicly available at <http://cdaweb.gsfc.nasa.gov>, instruments on the Advanced Composition Explorer (ACE) spacecraft measured, in near Earth space, that the solar wind density was about 4 particles cm^{-3} , the bulk solar wind velocity was about 600 km/s, and the ambient solar wind magnetic field was about 5 nT. The solar wind would have taken approximately 2 days to travel from the Earth to Mars during this time so the conditions just mentioned are likely to have existed in the solar wind near Mars on September 7. Furthermore, a qualitative inspection of MGS data for the interval from decimal day 250.263 to 250.266 shows that the interval

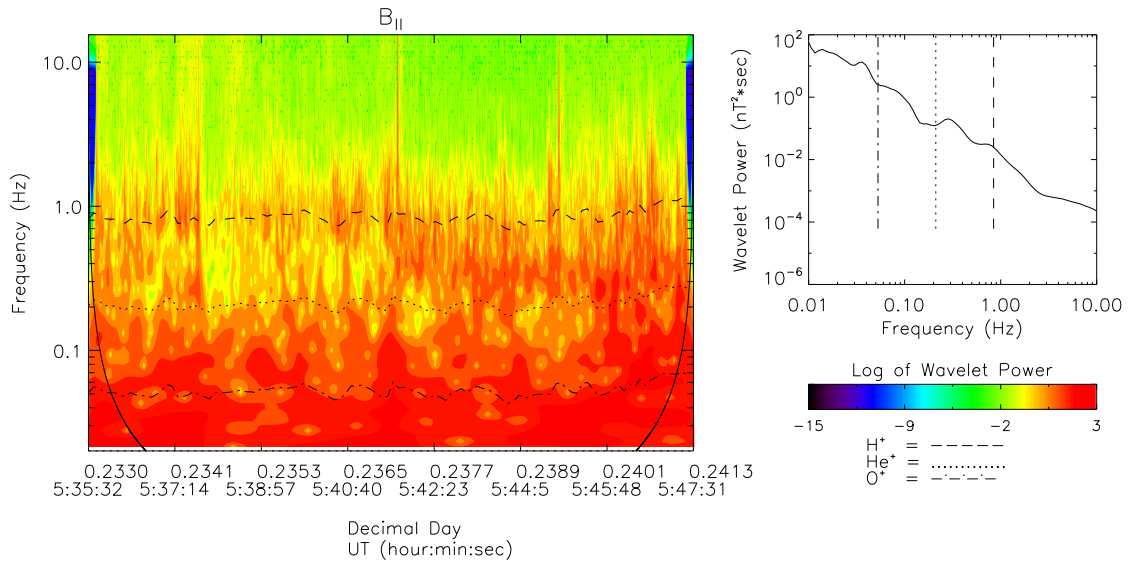


Figure 5.5: The same as figure 5.2 but for interval of 303.233 to 303.2413.

is typical for conditions on the Martian night side at 400 km. The mean $|B|$ for the interval is 10 nT and very small amplitude (< 1 nT) oscillations are noticeable in both the $B_{||}$ and B_{\perp} components. The expected error in the calibration of the MAG data is estimated to be as high as 0.5 nT on the night side so we regard with caution such small amplitude oscillations. Both the small size and the irregularity of the oscillations are typical for non-storm night side observations, although individual intervals do demonstrate both somewhat larger and somewhat smaller amplitude oscillations.

Figures 5.8, 5.9, and 5.10 show data from our last case example. This interval (dec-

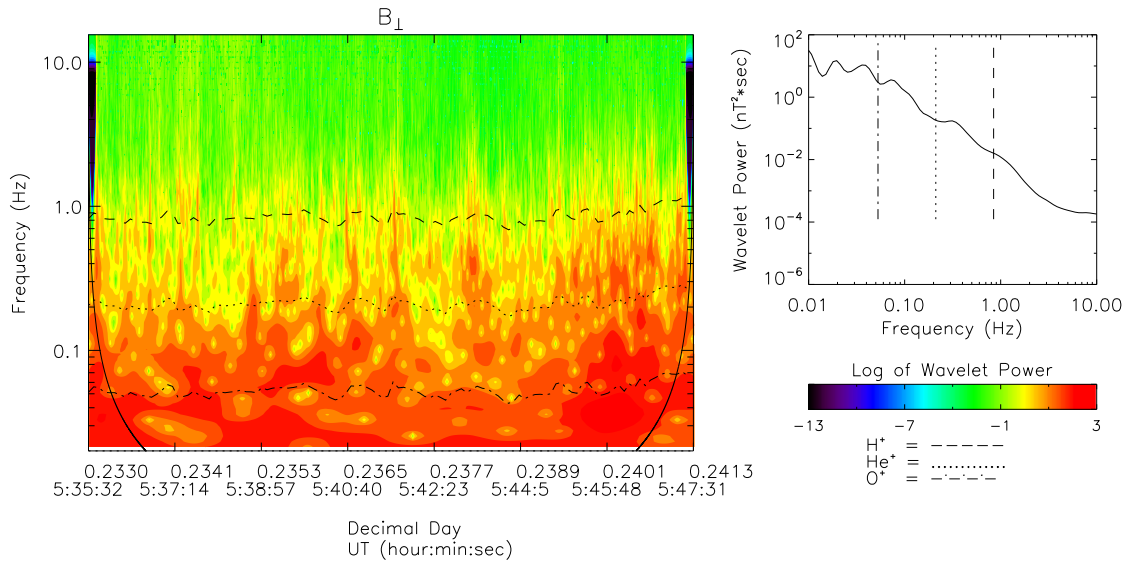


Figure 5.6: The same as figure 5.3 but for interval of 303.233 to 303.2413.

imal day 303.433 to 303.436) is from the day side MPR at about 60° SZA. Normally this region exhibits $|B|$ around 45 nT but during the passage of the solar storm this interval shows a $|B|$ of 140 nT. This increase in the magnetic field allows stronger perturbations to develop and we see large oscillations developing in the magnetic components and in the electron fluxes. These oscillations are much clearer than the smaller amplitude oscillations normally seen in this region and, unlike the previous case studies, show power across many frequencies with no distinct peaks. Spectral power is seen in both the B_{\parallel} and B_{\perp} components, as is normal for this region, but in this case the B_{\parallel} oscillations clearly dominate with spectral power at and below the

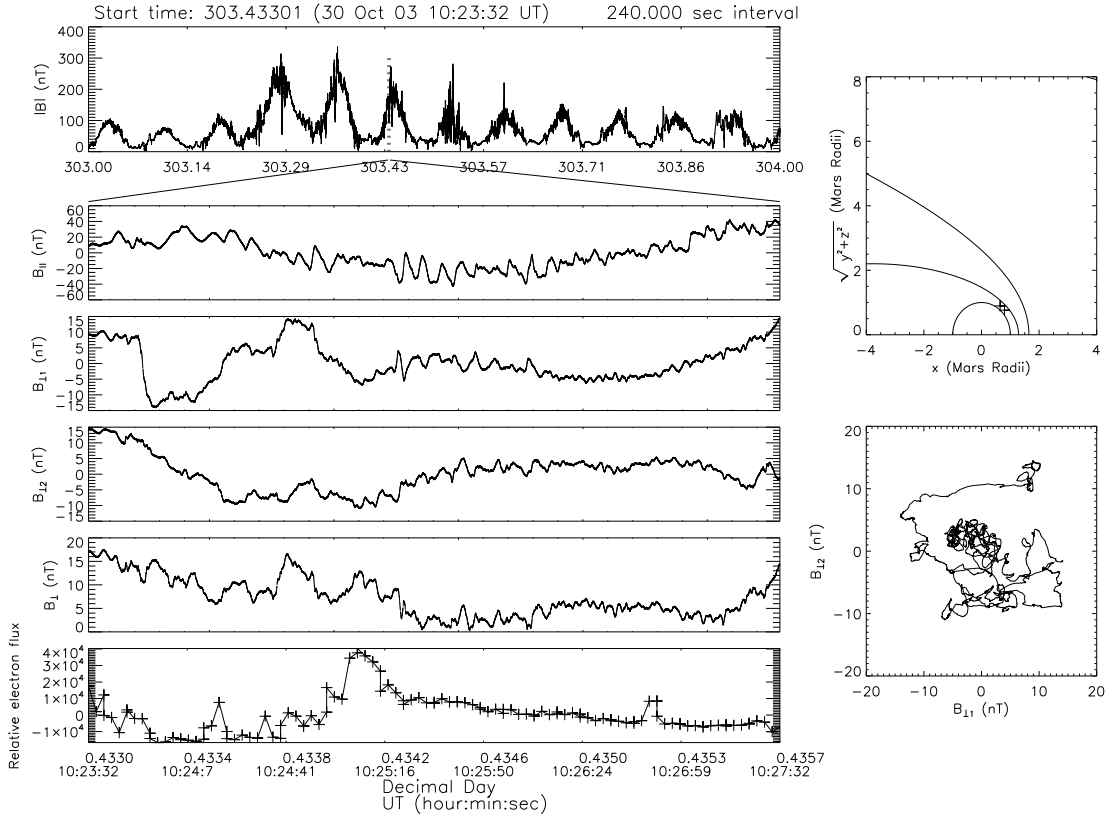


Figure 5.8: The same as figure 5.1 but for the interval of 303.433 to 303.436.

5.3 Discussion

The foregoing case studies and a qualitative examination of other intervals allow us to offer the following summary of our observations. In the day side MPR at 400 km during normal conditions, oscillatory activity is spread between the $B_{||}$ and B_{\perp} components although the $B_{||}$ components often offer greater spectral clarity and power. The greatest spectral power is present at frequencies at or below the hydrogen gyrofrequency. The passage of the solar storm serves to enhance the clarity and regularity of the oscillations, and although they continue to divide their power between components, the oscillations still often show greater spectral power in the $B_{||}$ com-

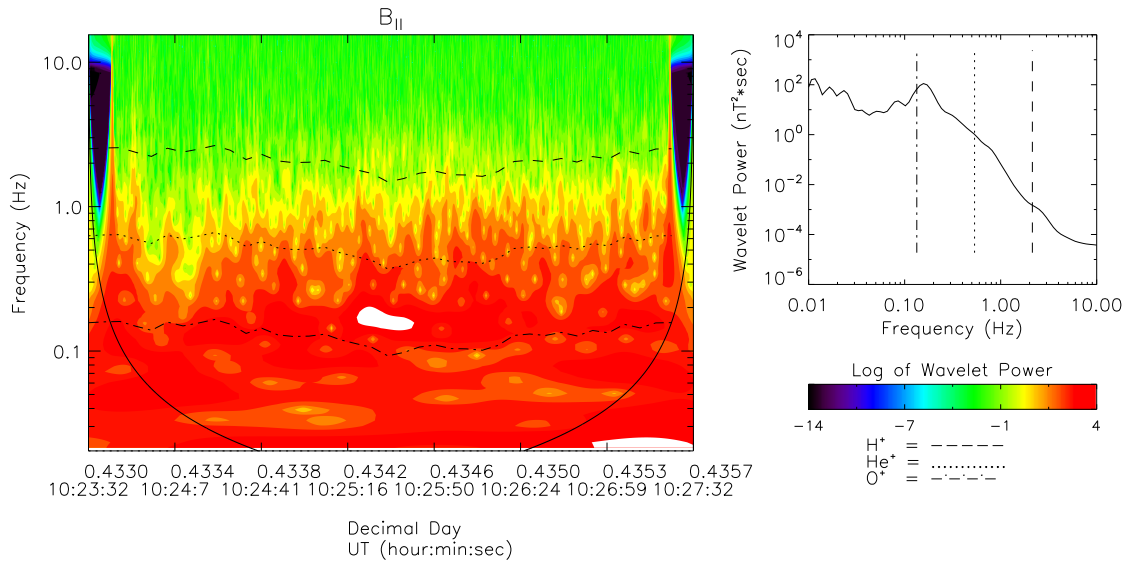


Figure 5.9: The same as figure 5.2 but for the interval of 303.433 to 303.436.

ponent. Individual intervals during the solar storm also are marked by propagation perpendicular to the background field and by anti-correlations between the electron fluxes and the B_{\parallel} components. These characteristics indicate the likely presence of mirror-mode instabilities since such instabilities exhibit many of the characteristics just enumerated [Gary, 1993]. Such instabilities may be generated by temperature anisotropies created as the enhanced solar wind from the solar storm compresses and penetrates the MPB [Crider *et al.*, 2004]. Such conditions may also allow for the convection of the mirror-mode instabilities from the magnetosheath where they have been observed to exist [Espley *et al.*, 2004]. Further work is required to fully

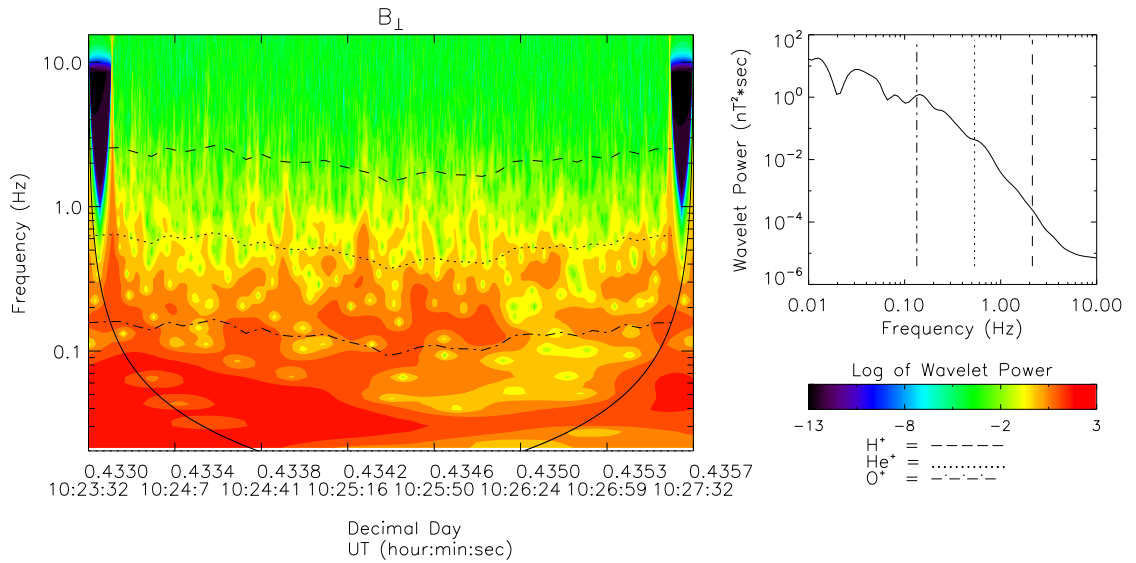


Figure 5.10: The same as figure 5.3 but for the interval of 303.433 to 303.436.

understand the physical origin of these instabilities.

On the night side at 400 km, we find that the general picture during the solar storm is very similar to the day side MPR (although $|B|$ is of course lower) with considerable spectral power divided between the B_{\parallel} and B_{\perp} components. Individual intervals during the solar storm's passage often show relatively powerful and regular B_{\parallel} fluctuations (and to a lesser extent B_{\perp} fluctuations) in contrast to the normally quiet conditions in this region. Some intervals show some correlations between the electron and the magnetic components and some intervals show a moderate degree of elliptical polarization. However, the most striking feature is the very clear signal

observed mainly in the B_{\parallel} component at the local proton gyrofrequency observed occasionally during the solar storm. Also, the strong spectral signal at or below the oxygen gyrofrequency is something not normally observable in this region. Unfortunately, a wide variety of plasma wave modes and instabilities have at least some of the characteristics that we observe in the region so identification of a single dominant wave mode is difficult without further measurements. Nonetheless, the clear evidence for spectral power at and below the oxygen gyrofrequency suggests the involvement of oxygen ions and/or heavier species (such as molecules such as O_2^+ , CO_2^+ , CO^+ , and N_2^+) in producing the oscillations observed. Such ions are most likely produced from the planetary neutral atmosphere. Escaping fluxes of such ions have been observed by Phobos 2 [Lundin *et al.*, 1989] and by Mars Express [Lundin *et al.*, 2004].

Likewise, during non-storm conditions wave activity associated with planetary pickup ions has been observed in the night side magnetosheath [Espley *et al.*, 2004]. By observing, during the passage of the solar storm, that such wave phenomena also occur in the normally placid tail region we show that atmospheric loss may occur across a larger spatial region during the passage of solar storms and that therefore enhanced rates of atmospheric loss may occur. This speculation is reinforced by the idea that the powerful compression caused by the passage of the solar storm is expected to cause larger segments of the planetary atmosphere to be exposed to the solar wind and hence subject to pickup mechanisms. It is an interesting question, which we leave to future research, as to the relative magnitudes of the total loss

throughout Martian history caused by the steady state interaction with the solar wind versus that caused by the enhanced episodic loss from strong solar activity.

Finally, we mention that in order to more fully understand the physical origin of the oscillations and in order to make a careful comparison with contemporary theory, we would want measurements of the pressures, temperatures, velocities, and densities of the plasma constituents. Fortunately, some of these measurements are available or derivable from observations made by the Mars Express (MEX) spacecraft which recently arrived at Mars [*Lundin et al.*, 2004]. Unfortunately, MEX had not yet arrived at Mars at the time of the solar storm examined in this work nor does it carry a magnetometer. Nonetheless, if similar solar storms arrive at Mars during MEX's lifetime (as previously noted the storm studied in this report was exceptionally large but significant if somewhat smaller solar storms are common on decadal timescales) then it should be possible to make intercomparisons between the MGS MAG/ER data and relevant MEX data from similar altitudes. We look forward to this opportunity and to also further study of interesting intervals from our current data set which were omitted for the sake of brevity in this report. Such studies will further our understanding of the physics involved in the passage of a large solar storm at Mars.

Chapter 6

Initial results from the ionosphere

I present here initial results of the first observations of low frequency fluctuations within the Martian ionosphere. The text is taken from the paper *Espley et al.* [2005b] with minor modifications for inclusion in this thesis (removing sections that duplicate previous material, etc.).

6.1 Introduction

Because Mars lacks an intrinsic planetary magnetic field, the solar wind interacts directly with the Martian ionosphere. However, patches of the Martian crust are highly magnetized and contribute to standing off the solar wind by the creation of mini-magnetospheres [*Acuña et al.*, 1998]. In the cases of the strongest crustal fields, the mini-magnetospheres protrude above the ionopause [*Brain et al.*, 2003] and protect the atmosphere that lies below them just as the Earth's global magnetosphere protects the terrestrial atmosphere from the solar wind. Interactions between the ionosphere, the solar wind, and the mini-magnetospheres produce a great deal of low frequency plasma fluctuations at altitudes greater than 800 km [*Espley et al.*,

2004]. Using data from Mars Global Surveyor's (MGS) magnetometer/electron reflectometer (MAG/ER) experiment, we present here initial observations of low frequency magnetic oscillations at ionospheric altitudes (approximately < 400 km).

These fluctuations are interesting for several reasons. By identifying or at least constraining which wave modes are present in a plasma, investigators are able to probe the temperature, density, composition, and pressure of a plasma. The Martian ionosphere has been the subject of several recent studies [*Shinagawa, 2000; Trotignon et al., 2000; Mitchell et al., 2001; Nagy et al., 2004; Lundin et al., 2004*] but further observations would be helpful. Such observations may be especially useful in understanding the ionospheric properties adjacent to and within the mini-magnetospheres. Furthermore, a wide variety of atmospheric phenomena, including dust storms and dust devils, are likely to produce low frequency electromagnetic noise which could potentially be fruitfully studied via in situ magnetic field observations [*Farrell et al., 1999*]. Lastly, an important geophysical exploration method, passive low frequency electromagnetic sounding, relies upon the existence of naturally occurring low frequency magnetic fluctuations. Specific varieties of this technique include the magnetotelluric technique [*Vozoff, 1991*] and magnetic gradiometry [*Pincon et al., 2000*]. We focus here on the magnetotelluric technique as an example of these methods. Demonstrating the plausibility of these techniques for use at Mars is one of the primary goals of this report.

The magnetotelluric technique (MT) is a passive electromagnetic sounding tech-

nique that has been used to great effect on Earth for geophysical exploration. Measuring the horizontal electric (E_x) and magnetic fields (H_y) (where the x and y subscripts simply indicate perpendicular cartesian coordinates) at the surface and taking their ratio indicates the conductivity structure of the subsurface, via the relation for ρ the apparent subsurface resistivity [cf. eqn. 8 in *Vozoff, 1991*]:

$$\rho(f) \propto \frac{1}{f} \left| \frac{E_x}{H_y} \right|^2 \quad (6.1)$$

As the wave frequency f decreases, the electromagnetic skin depth (the penetration of the wave into the subsurface) increases; hence a measurement of the horizontal components E_x and H_y yields the resistivity as a function of f , which can then be inverted into resistivity vs. depth. Highly conductive features such as liquid water stand out from more insulating host materials by at least several orders of magnitude. Note that water ice is significantly more resistive than liquid water hence would be rather difficult to distinguish from the surrounding rock. Therefore, any use of MT at Mars will need be accompanied by other techniques if a full subsurface characterization is to be accomplished. Figure 6.1 shows a schematic diagram illustrating the technique. *Grimm* [2002] laid out much of the theoretical framework necessary to use MT for subsurface sounding on Mars. As he noted, the small payload mass and power requirements for MT (which because its reliance on naturally occurring magnetic fluctuations does not require powered transmitters) and its depth of penetration (several hundreds of meters or greater) make it an important potential exploratory tool on

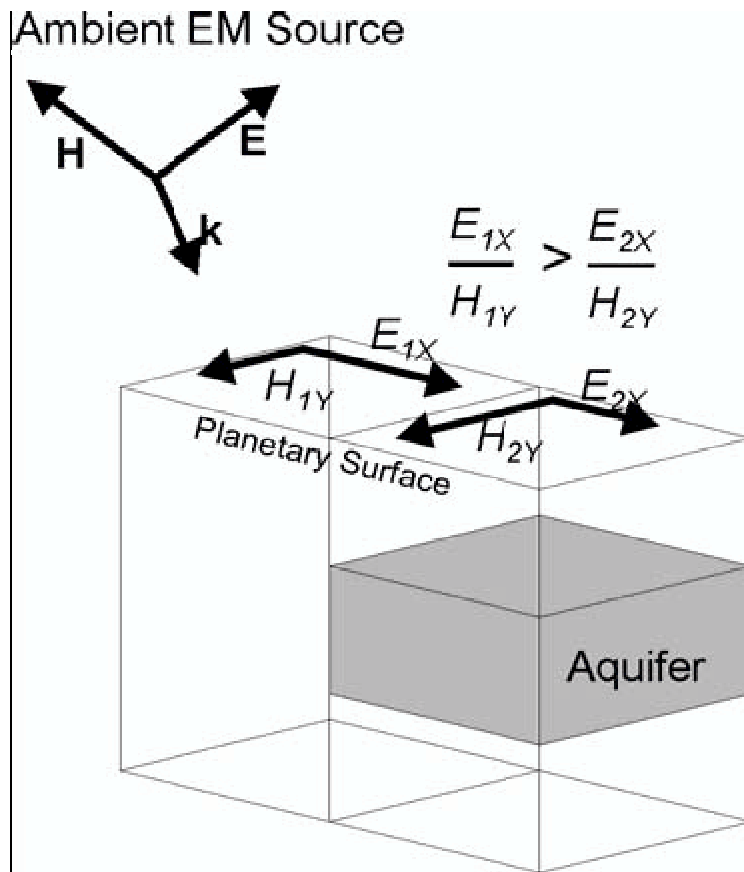


Figure 6.1: By measuring the ratio of the electric and magnetic field components of an EM wave at the surface, the subsurface conductivity can be determined. This occurs due to the finite skin depth of low-frequency waves in a typical subsurface, which will dissipate energy from the incident waves via direct currents. The ratio of E/H is known as the apparent impedance, and when measured as a function of frequency can be used to determine the depth and thickness of electrically conductive features such as liquid water. Natural EM emissions from the atmosphere and ionosphere are commonly used in this technique on Earth.

Mars. It could provide useful data regarding the distribution of subsurface liquid water which would have implications for the mystery of climate change at Mars, for the possibility of current or past Martian life, and for resource location for future human exploration.

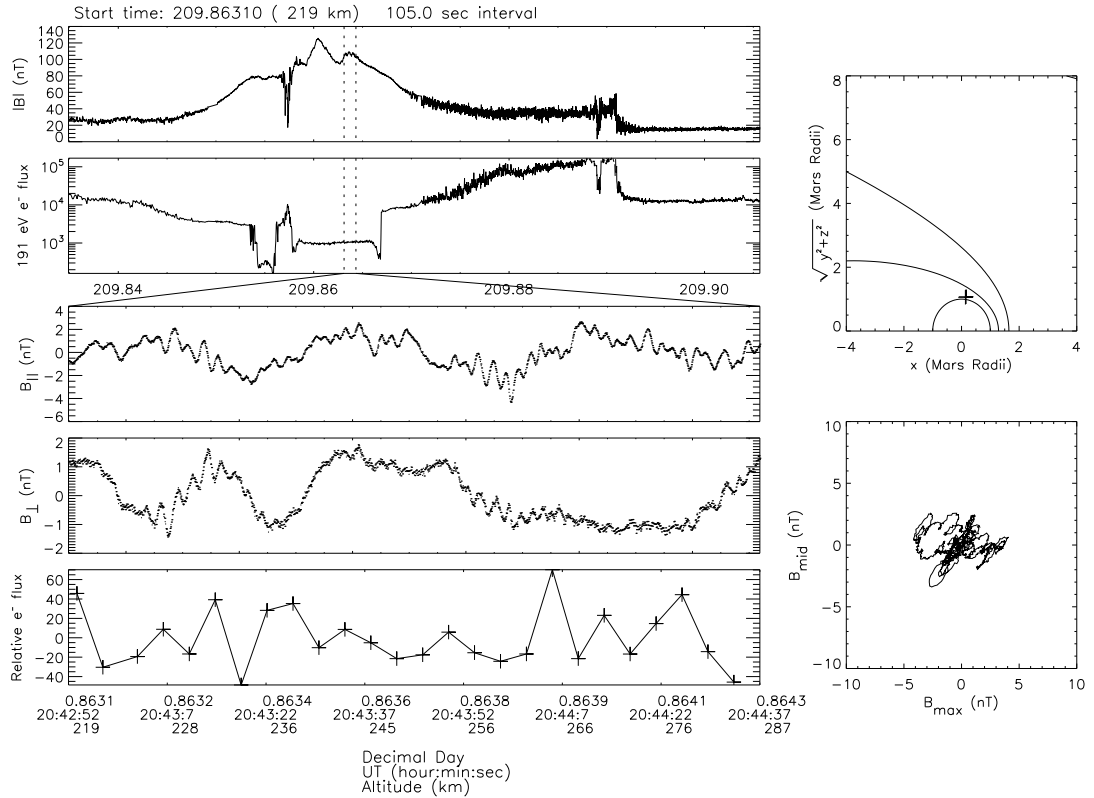


Figure 6.2: The magnetic fluctuations observed during a 105 second interval on the second periapsis of July 28, 1998 (decimal day 209). The top two panels show the magnetic field magnitude and 191 eV electron flux for the entire pass whereas the bottom three panels show, respectively, the parallel, perpendicular, and the relative electron flux fluctuations for the selected interval. The upper right panel shows the MGS location during the interval marked as a plus sign and the lower right panel shows the magnetic field components in the directions of the maximum and intermediate eigenvalues of the variance.

6.2 Results

We present here results from two different intervals. A systematic investigation of similar such intervals throughout the entire data set is under way and should yield results that allow for detailed statistics on the nature of the oscillations with respect to altitude, proximity to crustal sources, solar wind strength, and the diurnal cycle.

Figure 6.2 shows an example from the second periapsis of July 28, 1998 (decimal

day 209). The top two panels show $|B|$ and the 191 eV electron flux for the entire pass with dotted lines indicating the interval analyzed. The three panels below show, respectively, the B_{\parallel} , B_{\perp} , and the relative electron flux fluctuations. The upper right panel shows the location MGS (the starting and stopping locations nearly overlap on this scale and are marked by plus signs) during the interval analyzed. Also shown are the best fit locations of the bow shock and magnetic pileup boundary [*Vignes et al.*, 2000]. The panel in the lower right shows the magnetic field components in the directions of maximum and intermediate variance. Figures 6.3 and 6.4 show wavelet analyses of the same interval for the B_{\parallel} and B_{\perp} components. The left panels show the wavelet power spectra while the right panels show the global (time integrated) power spectra. Also marked on the wavelet power spectra are the cone of influence for numerical effects (the black near semi-circle) and contour lines indicating areas of spectral power that are 95% statistically significant [*Torrence and Compo*, 1998]. The local proton, helium, and oxygen gyrofrequencies are also marked on both the power spectra and the global spectra.

Since contextual ER data show (at approximately decimal day 209.857 and 209.867) the dropoff in flux characteristic of the photo-electron boundary associated with the ionopause [*Mitchell et al.*, 2001], it is reasonable that the analyzed interval is within the ionosphere. Coherent fluctuations (at altitudes between 219 and 287 km) are clearly seen in the parallel component and to a lesser extent in the perpendicular component. These observations were made at a solar zenith angle of approximately

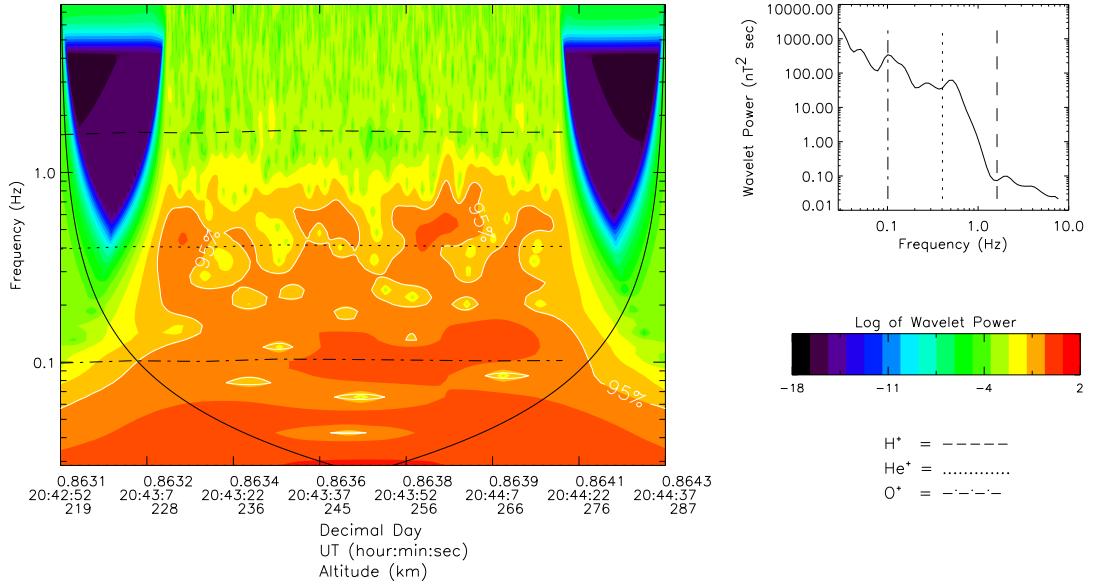


Figure 6.3: A wavelet analysis of the B_{\parallel} component for the interval shown in figure 6.2. The left panel shows a wavelet power spectrum with the color scale indicating spectral power. The right panel shows a global wavelet power spectrum for the interval. Superimposed on both figures are the local proton, helium, and oxygen gyrofrequencies. The semi-circular dark line indicates the minimum cone of influence for numerical edge effects [Torrence and Compo, 1998] though clearly for the short time series used here some additional numerical effects are present such as the large blue triangles of low spectral power on both edges. The white contour lines indicate areas of spectral power that are 95% statistically significant.

90° while MGS passed over the region approximately 160° east longitude and 81° north latitude - a region far from any of the significant crustal fields [Connerney *et al.*, 2001]. The average amplitudes of the B_{\parallel} and B_{\perp} fluctuations are, respectively 1.2 nT and 1.1 nT while the background field is 106 nT. The ratio of parallel to perpendicular spectral power is 1.7 for frequencies to 1 to 10 Hz, 7.7 for frequencies 0.1 to 1 Hz, and 0.91 for frequencies 0.01 to 0.1 Hz. Thus the waves can be charac-

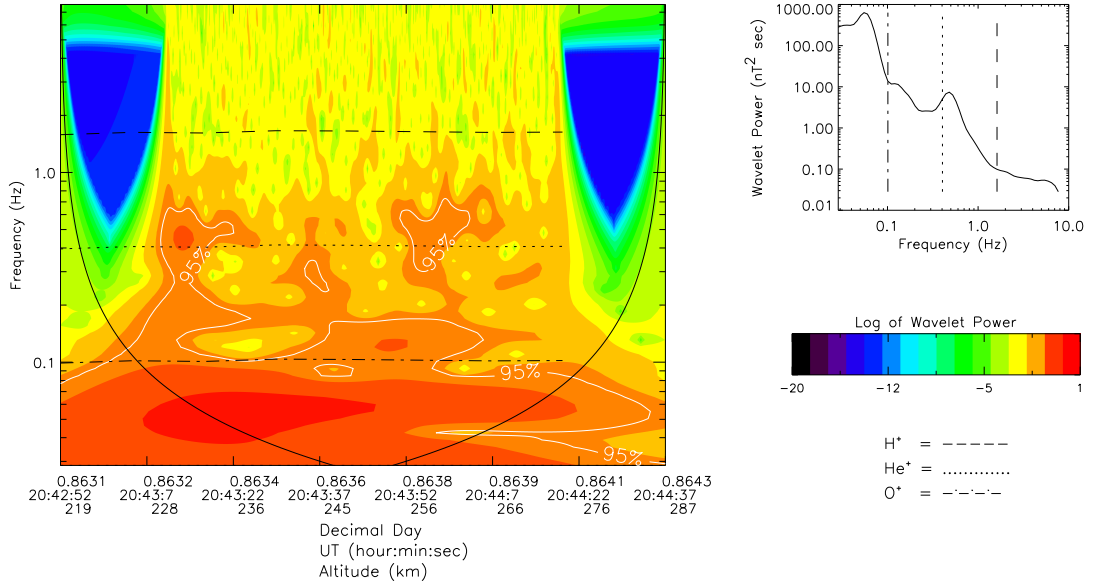


Figure 6.4: The same as figure 3 but for the B_{\perp} component.

terized as generally compressional especially at higher frequencies. The fluctuations are somewhat linearly polarized (0.46 ellipticity) as seen in the lower right panel of figure 2 and show neither a preference for right handed nor left handed polarization. The wave vector calculated is to be 83° from the direction of the mean magnetic field although the ratio of the eigenvalues is only 2.6 thus making this determination only marginally reliable. Correlation analysis shows nearly no correlation between the ER data and the MAG data (correlation coefficients of 0.01 and -0.14 respectively for the B_{\parallel} and B_{\perp} components) which is easily confirmed by a visual comparison of the data sparse ER time series and the MAG components.

Figure 6.3 shows that most clearly evident oscillations in the time series have spectral power between 0.08 and 0.6 Hz with a significant and relatively long-lived period of power at 0.1 Hz (nearly exactly at the oxygen gyrofrequency which is interesting since we are considering the parallel power). The large spectral power at frequencies as low as 0.03 Hz is reflective of the relatively large amplitude fluctuation evident in the time series that just barely makes 3 oscillations. Figure 6.4 shows that considerably less spectral power occurs in the perpendicular component, although some power is present at frequencies of 0.06 Hz and lower. There is also, near decimal day 209.8631, a series of clear peaks in evident in both the time series and as spectral power near 0.5 Hz.

Figures 6.5, 6.6, and 6.7 show another example, this time from December 16, 1998 (decimal day 350). In this case, MGS was passing over 340° east longitude and 40° north latitude which is just north of a significant crustal field. Because of the large amplitude signal from the crustal field (seen from approximately decimal day 350.164 to 350.169) obvious fluctuations are difficult to discern while MGS was directly over the crustal field. However, the interval just after the closest approach to the crustal field does show significant oscillations. Unfortunately, this is one of the orbits during which the ER instrument was turned off during closest approach due to safety concerns [Mitchell *et al.*, 2001], but nonetheless, we can see that at the tail end of our interval the ER flux greatly increases indicating MGS's passage through the ionopause.

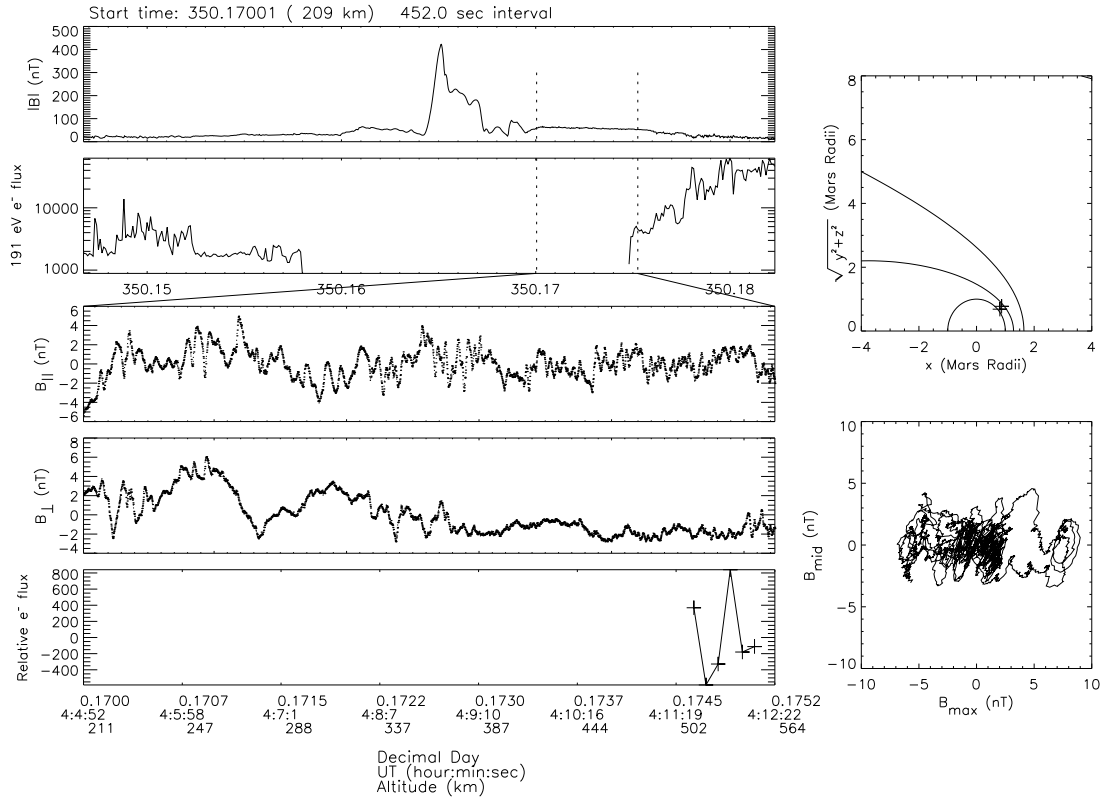


Figure 6.5: The same as figure 2 but for a 452 second interval during the first periapsis of December 16, 1998 (decimal day 350).

In the third and fourth panels of figure 6.5 we see fairly large amplitude, coherent oscillations in the directions both parallel and perpendicular to the mean magnetic field. Observations of these fluctuations start at an altitude of 209 km and continue past the ionopause (~ 520 km) well up into the magnetic pileup region. The average $|B|$ is 59 nT and the average amplitudes of the $B_{||}$ and B_{\perp} are 1.2 nT and 1.7 nT, respectively. These average amplitudes, measured from the time series data, are strongly dependent on the lowest frequency fluctuations present. The ratio of parallel and perpendicular spectral power is 1.4 for frequencies 1 to 10 Hz, 5.5 for frequencies 0.1 to 1 Hz, 0.43 for frequencies 0.01 to 0.1 Hz, and 0.30 for frequencies 0.001 to 0.01

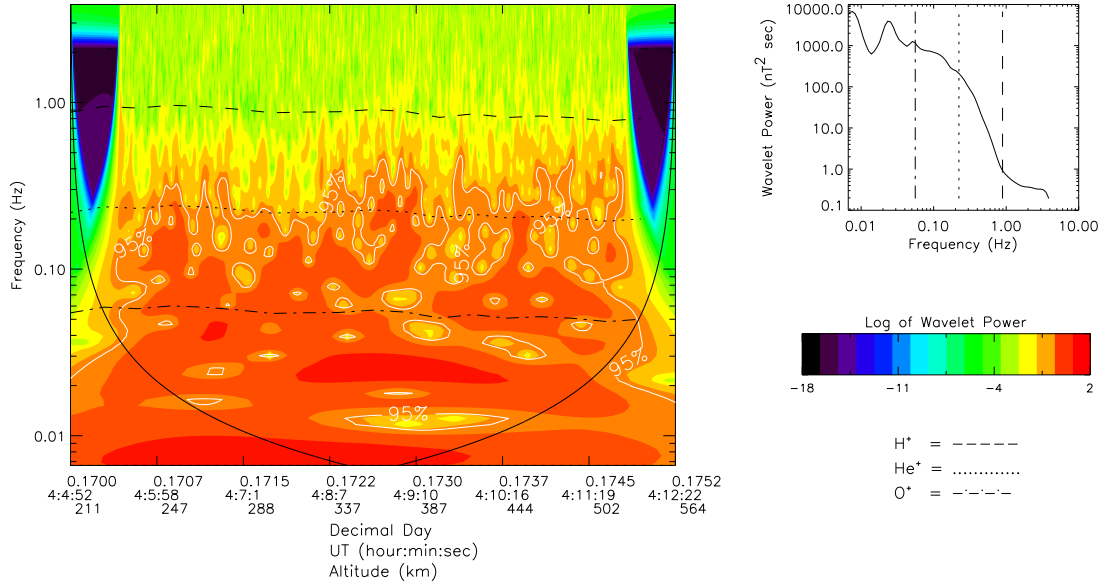


Figure 6.6: The same as figure 6.3 but for the same interval as figure 6.5.

Hz. Thus the waves are predominately transverse only for lower frequencies and, in fact, figures 6.6 and 6.7 show that this low frequency transverse predominance also only occurs for the lowest altitudes. This can be confirmed by an inspection of the time series of the B_{\perp} fluctuations that shows them to be relatively damped at altitudes higher than 350 km. There is a strong peak in the B_{\parallel} at 0.02 Hz and generally most of the spectral power, for both components, is between 0.02 and 0.2 Hz except for the lowest frequency power which is dominated by the peak at 0.008 Hz in B_{\perp} . This interval is more linearly polarized (ellipticity of 0.14) than the previous, shows no preference for right or left handed polarization, and does not have a well constrained

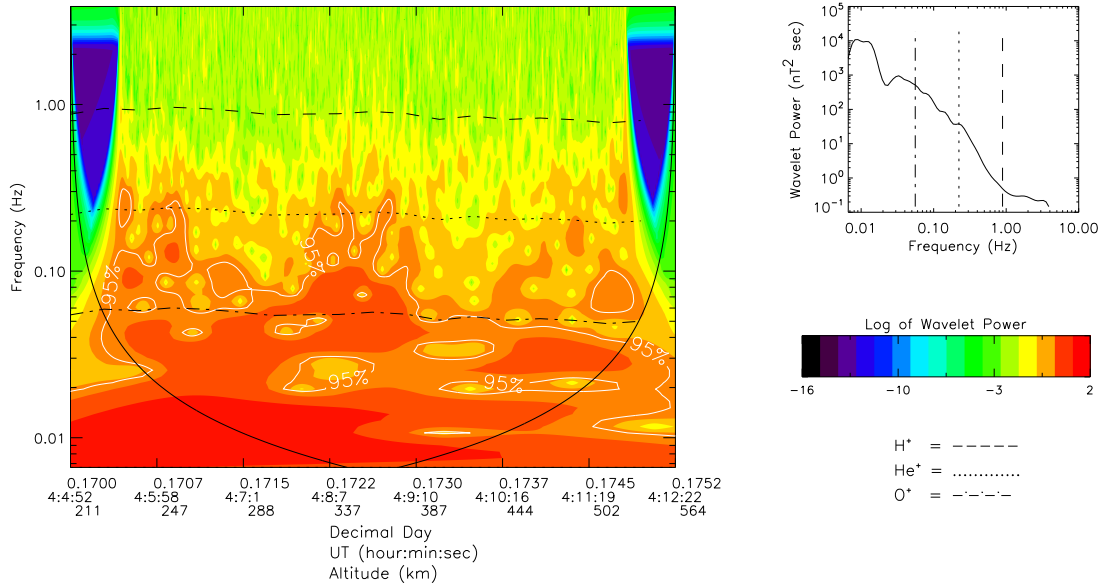


Figure 6.7: The same as figure 6.4 but for the same interval as figure 6.5.

wave vector (the eigenvalue ratio is 1.1). No significant ER-MAG correlation can be observed due to the lack of ER data for the majority of the interval.

6.3 Discussion

Several important inferences can be drawn even from these initial observations. We have qualitatively examined many other intervals besides the ones shown here and these intervals do not seem abnormal. A more detailed statistical study is underway.

First, there is significant spectral power at low altitude at frequencies of 0.01 to 1 Hz. This is a viable frequency regime for MT methods. Secondly, significant oscil-

lations have been identified both close to and far from crustal field sources. Further study is needed to determine systematic differences, if any, between oscillations near to and far from the crustal fields. However, the current observations indicate, at least, the plausibility of using MT methods across the entire planet and not just near crustal fields (which are clustered predominantly in the cratered southern highlands).

Identifying the various waves modes present would assist us in understanding the physical origin of the waves observed and in understanding how the plasma parameters (such as density and β , the ratio of plasma pressure to magnetic pressure) vary with altitude. Unfortunately, a wide variety of waves modes is likely to be present with some waves originating in the ionospheric plasma and some propagating from the solar wind into the ionosphere thus making a precise identification in terms of theoretical modes difficult. Nonetheless, the waves shown in our two examples have properties consistent with the obliquely propagating magnetosonic wave identified theoretically by *Gary* [1993]. This mode is calculated using Vlasov theory for a uniform plasma and is found to be lightly damped for both low and high β for the lowest frequencies. As the frequency of the mode increases to frequencies at and just below the proton gyrofrequency, the damping decreases for $\beta < 4$ [cf. section 6.2 of *Gary*, 1993]. Our observations show that the predominant waves are compressional and, assuming negligible Doppler shift from the relatively slow moving ionospheric plasma, and are observed in approximately the plasma frame with frequencies that are below but within an order of magnitude of the local proton gyrofrequency. One

aberrant characteristic of the observed fluctuations is that the plasma and magnitude field fluctuations are not correlated whereas in the theoretical magnetosonic mode they are correlated. This discrepancy could be explained by the relative sparseness of the ER data which makes true correlations difficult to detect, especially at the higher frequencies.

The kinetic magnetosonic wave mode also has the fastest phase speed of the modes identified using Vlasov theory and therefore is associated with the MHD fast mode identified using fluid theory [*Krauss-Varban et al.*, 1994]. Such fast mode waves have been identified as one of the primary mechanisms for producing the low frequency magnetic fluctuations used for MT methods on Earth. Solar wind fluctuations couple with the Earth's planetary magnetic field to produce what are termed cavity modes [*Kivelson and Southwood*, 1988]. Unaltered, this physical model will not correctly explain the propagation of low frequency waves at Mars since it depends on the terrestrial global magnetic field. However, fast mode waves have been identified at Mars by *Bertucci et al.* [2004] just downstream of the magnetic pileup boundary which has an approximate altitude of 700 km. Furthermore, work has been done trying to understand the propagation of low frequency waves through the terrestrial ionosphere to the ground [*Hughes and Southwood*, 1976]. Such work may be applicable to Mars. A fully developed model for the production and propagation of such waves is left for future work. This current report serves to identify such waves and to point out the plausibility of their use in a magnetotelluric survey of the Martian subsurface.

Chapter 7

Concluding Remarks

In the preceding chapters, I have attempted to provide observations of low frequency plasma waves in a variety of locations in the near Mars space, and to provide some physical interpretations of these observations. I provide a summary of these results, discuss some of the implications of this information, and discuss areas for future work.

We have learned that in the dayside magnetosheath, mirror mode waves are the most likely type of fluctuation. These instabilities develop from temperature anisotropies associated with plasma depletion layers. These waves serve as a mechanism for re-establishing isotropy. Waves in the nightside magnetosheath are generally caused by the interaction of the solar wind with planetary ions. These resonant ion cyclotron waves are an indirect observation of ongoing atmospheric loss at Mars. Such loss is of great interest given its connection to climate change [*Jakosky and Phillips, 2001*]. Observations of the associated plasma waves does not seem able to give a direct estimate of the numbers of ions being lost per second (a number of great interest to a number of scientific communities). However, when combined with other observations

(such as those available from instruments on Mars Express[Lundin *et al.*, 2004]) and with current modelling efforts, observations of resonant ion cyclotron waves should help paint a more complete picture of atmospheric loss at Mars.

For both the dayside and nightside magnetosheath fluctuations, it seems that the observations are out ahead of the theory. On the one hand, the high β nature of the region makes traditional MHD theories inadequate but on the other hand nonlinear kinetic theories have yet to be developed. I am interested in pursuing collaborations with theorists to develop a set of theoretical results specific to the conditions at Mars.

Observations during the large solar storms of October 2003 showed that the low frequency plasma waves are dramatically altered during such a storm. Clear resonant features are observed even in the normally placid magnetotail. I have speculated whether such large solar storms may cause episodic, massive atmospheric loss that rivals the steady state atmospheric loss. Initial collaborations have been started with modelers interested in modeling such extreme events. Further large storm events may be able to be monitored by both Mars Express' plasma instruments and MGS' magnetometer. Such collaborative efforts should yield more information on the changes caused by the solar storms.

Initial observations of low frequency oscillations in the ionosphere have been presented. Such initial efforts show that the ionosphere is likely to be full of interesting low frequency phenomena. They also help establish the plausibility of using the technique of magnetotellurics for subsurface sounding. Using such a technique is of great

interest since it will help establish the history of water and help locate resources for robotic and human exploration. Efforts to continue the characterization of waves in the ionosphere are underway.

Other interesting projects await time and energy from myself or other researchers. Low frequency plasma waves at Venus have yet to be fully explored, particularly at lower altitudes. It may be that the techniques that I have developed here can be used to explore the low frequency plasma waves of the Venusian magnetosheath. The data from Mars has many tens of thousands of intervals that hold individual stories that are glossed over in the statistical results I have presented here. Interesting science is bound to be found if detailed analysis of even a few of these intervals is undertaken.

The study of low frequency plasma waves has proven to be a rich and interesting scientific topic. I hope to continue the exploration of this topic and related ones, and I believe the results contained in this thesis represent a useful beginning to this exploration.

Bibliography

Acuña, M. H., J. E. P. Connerney, P. Wasilewski, R. P. Lin, K. A. Anderson, C. W. Carlson, J. McFadden, D. W. Curtis, D. Mitchell, H. Reme, C. Mazelle, J. A. Sauvaud, C. D'Uston, A. Cros, J. L. Medale, S. J. Bauer, P. Cloutier, M. Mayhew, D. Winterhalter, and N. F. Ness (1998), Magnetic field and plasma observations at Mars: Initial results from the Mars Global Surveyor Mission, *Science*, *279*, 1676-1680.

Acuña, M. H., J. E. P. Connerney, P. Wasilewski, R. P. Lin, D. Mitchell, K. A. Anderson, C. W. Carlson, J. McFadden, H. Reme, C. Mazelle, D. Vignes, S. J. Bauer, P. Cloutier, and N. F. Ness (2001), Magnetic field of Mars: Summary of results from the aerobraking and mapping orbits, *J. Geophys. Res.*, *106*, 23,403-23,417.

Albee, A. L., R. E. Arvidson, F. Palluconi, and T. Thorpe (2001), Overview of the Mars Global Surveyor mission, *J. Geophys. Res.*, *106*, 23,291-23,316.

Arthur, C. W., R. L. McPherron, and J. D. Means (1976), A comparative study of three techniques for using the spectral matrix in wave analysis, *Radio Science*, *11*, 10, 833-845.

Bertucci, C. (2003), Study of the interaction of the solar wind with Mars: Implications on the atmospheric escape mechanisms, Ph.D. Thesis, 280 pp., Paul Sabatier University (Toulouse III), Toulouse, France, December 2003.

Bertucci, C., C. Mazelle, J. A. Slavin, C. T. Russell, and M. H. Acuña (2003), Mag-

netic field draping enhancement at Venus: Evidence for a magnetic pileup boundary, *Geophys. Res. Lett.*, *30*, 1876, doi:10.1029/2003GL017271.

Bertucci, C., C. Mazelle, D. H. Crider, D. L. Mitchell, K. Sauer, M. H. Acuña, J. E. P. Connerney, R. P. Lin, N. F. Ness, and D. Winterhalter (2004), MGS MAG/ER observations at the magnetic pileup boundary of Mars: Draping enhancement and low frequency waves, *Adv. Space Res.*, *33*, 1938-1944.

Brace, L. H., R. C. Elphic, and S. A. Curtis (1983), Wave structure in the Venusian nightside ionosphere, *Geophys. Res. Lett.*, *10*, 1116-1119.

Brain, D. A., F. Bagenal, M. H. Acuña, J. E. P. Connerney, D. H. Crider, C. Mazelle, D. L. Mitchell, and N. F. Ness (2002), Observations of low-frequency electromagnetic plasma waves upstream from the Martian shock, *J. Geophys. Res.*, *107*(A6), SMP 9-1, doi:10.1029/2000JA000416.

Brain, D. A., F. Bagenal, M. H. Acuña, and J. E. P. Connerney (2003), Martian magnetic morphology: Contributions from the solar wind and crust, *J. Geophys. Res.*, *108* (A12), 1424, doi:10.1029/2002JA009482.

Chen, Y. and P. A. Cloutier (2003), Martian hydrogen exosphere charge exchange with solar wind, *J. Geophys. Res.*, *108*(A10), 1381, doi:10.1029/2002JA009604.

Cloutier, P. A., C. C. Law, D. H. Crider, P. W. Walker, Y. Chen, M. H. Acuña, J. E. P. Connerney, R. P. Lin, K. A. Anderson, D. L. Mitchell, C. W. Carlson, J.

McFadden, D. A. Brain, H. Reme, C. Mazelle, J. A. Sauvand, C. d'Uston, D. Vignes, S. J. Bauer, and N. F. Ness(1999), Venus-like interaction of the solar wind with Mars, *Geophys. Res. Lett.*, *26*, 2685-2688.

Connerney, J. E. P., M. H. Acuña, P. J. Wasilewski, G. Kletetschka, N. F. Ness, H. Reme, R. P. Lin, and D. L. Mitchell (2001), The Global Magnetic Field of Mars and Implications for Crustal Evolution, *Geophys. Res. Lett.*, *28*, 4015-4018.

Crider, D. H. (1999), Evidence of electron impact ionization in the magnetic pileup boundary of Mars – Observations and modeling results, Ph.D. thesis, 109 pp., Rice Univ., Houston, TX, May 1999.

Crider, D. H., D. Vignes, A. M. Krymskii, T. K. Breus, N. F. Ness, D. L. Mitchell, J. A. Slavin, and M. Acuña (2003), A proxy for determining solar wind dynamic pressure at Mars using Mars Global Surveyor data, *J. Geophys. Res.*, *108(A12)*, 1461, doi:10.1029/ 2003JA009875.

Crider, D. H., J. R. Espley, D. A. Brain, D. L. Mitchell, J. E. P. Connerney, M. H. Acuña (2005), Mars Global Surveyor observations of the October 2003 solar super-storm's encounter with Mars, accepted in *J. Geophys. Res.*, doi:10.1029/2004JA010881.

Crooker, N. U., and G. L. Siscoe (1977), A Mechanism for Pressure Anisotropy and Mirror Instability in the Dayside Magnetosheath, *J. Geophys. Res.*, *82*, 185-186.

Delva, M. and E. Dubinin (1998), Upstream ULF fluctuations near Mars, *J. Geophys. Res.*, *103*, 317-326.

Dubinin, E., K. Sauer, J. F. McKenzie, and G. Chanteur (2003), Solitons, oscillitons, and stationary waves in a warm p - alpha plasma, *J. Geophys. Res.*, *108*(A7), 1296, doi:10.1029/2002JA009572.

Dubinin, E., K. Sauer, and J. F. McKenzie (2004), Nonlinear stationary waves and solitons in ion beam-plasma configuration, *J. Geophys. Res.*, *109*, A02208, doi:10.1029/2003JA010283.

Espley, J. R., P. A. Cloutier, D. A. Brain, D. H. Crider, M. H. Acuña (2004), Observations of low frequency magnetic oscillations in the Martian magnetosheath, magnetic pileup region, and tail, *J. Geophys. Res.*, *109*, A07213, doi:10.1029/2003JA010193.

Espley, J. R., P. A. Cloutier, D. H. Crider, D. A. Brain, , M. H. Acuña (2005a), Low frequency plasma oscillations at Mars during the October 2003 solar storm, *J. Geophys. Res.*, *110*, A09S33, doi:10.1029/2004JA010935.

Espley, J. R., G. T. Delory, P. A. Cloutier (2005b), Initial observations of low frequency magnetic fluctuations in the Martian ionosphere, submitted to *J. Geophys. Res.*

Farrell, W. M., M. L. Kaiser, M. D. Desch, J. G. Houser, S. A. Cummer, D. M. Wilt, G. A. Landis (1999), Detecting electrical activity from Martian dust storms, *J. Geophys. Res.*, *104*, E2, 3795-3801.

Gary, S. P. (1991), Electromagnetic Ion/Ion Instabilities and Their Consequences in Space Plasmas: A Review, *Space Sci. Rev.*, *56*, 373-415.

- Gary, S. P. (1992), The Mirror and Ion Cyclotron Anisotropy Instabilities, *J. Geophys. Res.* *97*, 8519-8529.
- Gary, S. P. (1993), *Theory of space plasma microinstabilities*, Cambridge University Press, New York.
- Gary, S. P., S. A. Fuselier, and B. J. Anderson (1993), Ion Anisotropy Instabilities in the Magnetosheath, *J. Geophys. Res.*, *98*, 1481-1488.
- Glassmeier, K.-H., and F. M. Neubauer (1993), Low-Frequency Electromagnetic Plasma Waves at Comet P/Grigg-Skjellerup: Overview and Spectral Characteristics, *J. Geophys. Res.*, *98*, 20,921-20,935.
- Glassmeier, K.-H., F. M. Neubauer, M. H. Acuña, and F. Mariani (1987), Low-frequency magnetic field fluctuations in comet P/Halley's magnetosheath: Giotto observations, *Astron. Astrophys.*, *187*, 65-68.
- Glassmeier, K.-H., U. Motschmann, C. Mazelle, F. M. Neubauer, K. Sauer, S. A. Fuselier, and M. H. Acuña (1993), Mirror Modes and Fast Magnetosonic Waves Near the Magnetic Pileup Boundary of Comet P/Halley, *J. Geophys. Res.*, *98*, 20,955-20,964.
- Grard, R., A. Pedersen, S. Klimov, S. Savin, A. Skalsky, J. G. Totignon, and C. Kennel (1989), First measurements of plasma waves near Mars, *Nature*, *341*, 607-609.
- Grebowsky, J. M., D. H. Crider, D. S. Intriligator, R. E. Hartle, and M. H. Acuña

- (2004), Venus/Mars pickup ions and ionosheath wave structures, *Adv. Space Res.*, *33*, 176-181.
- Grimm, R. E. (2002), Low-frequency electromagnetic exploration for groundwater on Mars, *J. Geophys. Res.*, *107*(E2), 5006, doi:10.1029/2001JE001504.
- Hausman, B. A., F. C. Michel, J. R. Espley, and P. A. Cloutier (2004), On determining the nature and orientation of magnetic directional discontinuities: Problems with the minimum variance method, *J. Geophys. Res.*, *109*, A11102, doi:10.1029/2004JA010670.
- Huba, J. D. (1998), NRL Plasma Formulary: Revised, Office of Naval Research, Washington, DC.
- Huba, J. D., and R. J. Strangeway (1997), Plasma wave phenomena at Venus, in *Venus II*, edited by S. W. Bougher, D. M. Hunten, and R. J. Phillips, pp. 95-124, Univ. of Ariz. Press, Tucson.
- Hubert, D., Nature and origin of wave modes in the dayside Earth magnetosheath (1994), *Adv. Space Res.*, *14*, 6, 55-64.
- Hughes, W. J. and D. J. Southwood (1976), The screening of micropulsation signals by the atmosphere and ionosphere, *J. Geophys. Res.*, *81*(19), 3234-3240.
- Ip, W-H., and I. Axford (1990), The Plasma, in *Physics and Chemistry of Comets*, edited by W. F. Huebner, pp. 177-233, Springer-Verlag, Berlin.

- Jakosky, B. M. and R. J. Phillips (2001), Mars' volatile and climate history, *Nature*, *412*, 237-244.
- Kivelson, M. G. (1995), Pulsations and magnetohydrodynamic waves, in *Introduction to Space Plasma Physics*, ed. M. G. Kivelson and C. T. Russell, Cambridge University Press, New York.
- Kivelson, M. G. and D. J. Southwood (1988), Hydromagnetic waves and the ionosphere, *Geophys. Res. Lett.*, *15*, 1271-1274.
- Knetter, T., F. M. Neubauer, T. Horbury, and A. Balogh (2003), Discontinuity observations with Cluster, *Adv. Space Res.*, *32*, 543.
- Krauss-Varban, D., N. Omidi, and K. B. Quest (1994), Mode properties of low-frequency waves: Kinetic theory versus Hall-MHD, *J. Geophys. Res.*, *99*, 5987-6009.
- Lacombe, C. and G. Belmont (1995), Waves in the Earth's magnetosheath: observations and interpretations, *Adv. Space Res.*, *15*, 8/9, 329-340.
- Lee, M. A. (1989), Ultra-low frequency waves at comets, in *Plasma Waves and Instabilities at Comets and in Magnetospheres*, *Geophys. Monogr. Ser.*, vol. 53, edited by B. T. Tsurutani and H. Oya, pp. 13-30, AGU, Washington, D. C.
- Luhmann, J. G., M. Tatrallyay, C. T. Russell, and D. Winterhalter (1983), Magnetic field fluctuations in the Venus magnetosheath, *Geophys. Res. Lett.*, *10*, 655-658.

Luhmann, J. G., C. T. Russell, and J. L. Phillips (1987), On the Role of the Quasi-Parallel Bow Shock in Ion Pickup: A Lesson from Venus?, *J. Geophys. Res.*, *92*, 2544-2550.

Luhmann, J. G., S. A. Ledvina, and C. T. Russell (2004), Induced magnetospheres, *Adv. Space Res.*, *33*(11), 1905-1912.

Lundin, R., et al. (2004), Solar Wind-Induced Atmospheric Erosion at Mars: First Results from ASPERA-3 on Mars Express, *Science*, *305*, 1933-1936.

Lundin, R. et al. (2004), Solar Wind-Induced Atmospheric Erosion at Mars: First Results from ASPERA-3 on Mars Express, *Science*, *305*, 1933-1936.

Mazelle, C., G. Belmont, K.-H. Glassmeier, D. Le Queau, and H. Reme (1991), Ultra low frequency waves at the magnetic pile-up boundary of comet P/Halley, *Adv. Space Res.*, *11*(9), 73-77.

Mazelle, C., H. Reme, F. M. Neubauer, K.-H. Glassmeier (1995), Comparison of the main magnetic and plasma features in the environments of comets Grigg-Skjellerup and Halley, *Adv. Space Res.*, *16*(4), 41-45.

McPherron, R. L., C. T. Russell, and P. J. Coleman, Jr. (1972), Fluctuating magnetic fields in the magnetosphere, 2, ULF waves, *Space Sci. Rev.*, *13*, 411-454.

Means, J. D. (1972), Use of the three-dimensional covariance matrix in analyzing the polarization properties of plane waves, *J. Geophys. Res.*, *77*, 5551-5559.

Mitchell, D. L., R. P. Lin, H. Reme, D. H. Crider, P. A. Cloutier, J. E. P. Connerney, M. H. Acuña, and N. F. Ness (2000), Oxygen Auger electrons observed in Mars' ionosphere, *Geophys. Res. Lett.*, *27*, 18711874.

Mitchell, D. L., R. P. Lin, C. Mazelle, H. Rème, P. A. Cloutier, J. E. P. Connerney, M. H. Acuña, and N. F. Ness (2001), Probing Mars' crustal magnetic field and ionosphere with the MGS Electron Reflectometer, *J. Geophys. Res.*, *106*, 23,419-23,427.

Nagy, A. F., et al. (2004), The Plasma Environment of Mars, *Space Sci. Rev.*, *111* 33-114.

Neubauer, F. M., K.-H. Glassmeier, M. Pohl, J. Raeder, M. H. Acuña, L. F. Burlaga, N. F. Ness, G. Musmann, F. Mariani, M. K. Wallis, E. Ungstrup, and H. U. Schmidt (1986), First results from the Giotto Magnetometer Experiment at Comet Halley, *Nature*, *321*, 352-355.

Neubauer, F. M., K.-H. Glassmeier, A. J. Coates, and A. D. Johnstone (1993), Low-Frequency Electromagnetic Plasma Waves at Comet P/Grigg-Skjellerup: Analysis and Interpretation, *J. Geophys. Res.*, *98*, 20,937-20,953.

Oieroset, M., D. L. Mitchell, T. D. Phan, R. P. Lin, D. H. Crider, and M. H. Acuña (2004), The magnetic field pile-up and density depletion in the Martian magnetosheath: A comparison with the plasma depletion layer upstream of Earth's magnetopause, *Space Sci. Rev.*, *111*, 185-202.

- Orlowski, D. S., G. K. Crawford, and C. T. Russell (1990), Upstream waves at Mercury, Venus, and Earth - Comparison of the properties of one Hertz waves, *Geophys. Res. Lett.*, *17*, 2293-2296.
- Orlowski, D. S., C. T. Russell, D. Krauss-Varban, and N. Omidi (1994), A test of the Hall-MHD model: Application to low-frequency upstream waves at Venus, *J. Geophys. Res.*, *99*, 169-178.
- Omidi, N., A. O'Farrell, and D. Krauss-Varban, Sources of magnetosheath waves and turbulence (1994), *Adv. Space Res.*, *14*, 6, 45-54.
- Pincon, J. L., M. Menvielle, and L. Szarka (2000), Geomagnetic induction study using the NetLander network of magnetometers, *Planet. Space Sci.*, *48*, 1261.
- Press, W. H., S. A. Teukolsky, W. T. Vetterling, and B. P. Flannery (1992), Chapter 14: Statistical Description of Data, in *Numerical Recipes in Fortran*, 2nd ed., 963 pp., Cambridge University Press, New York.
- Rankin, D. and R. Kurtz, Statistical study of micropulsation polarizations (1970), *J. Geophys. Res.*, *75*, 5444-5458.
- Riedler, W., K. Schwingenschuh, D. Moehlmann, V. N. Oraevskii, E. Eroshenko, and J. Slavin (1989), Magnetic fields near Mars: First results, *Nature*, *341*, 604-607.
- Russell, C. T., J. G. Luhmann, K. Schwingenschuh, W. Riedler, and Y. Yeroshenko (1990), Upstream waves at Mars: Phobos observations, *Geophys. Res. Lett.*, *17*, 897-900.

- Russell, C. T., J. G. Luhmann, K. Schwingenschuh, W. Riedler, and Y. Yeroshenko (1992), Upstream waves at Mars, *Adv. Space Res.*, *12*, 251-254.
- Sagdeev, R. Z., V. D. Shapiro, V. I. Shevchenko, A. Zaiharov, P. Kiraly, K. Szego, A. F. Nagy, and R. J. Grard (1990), Wave activity in the neighborhood of the bow shock of Mars, *Geophys. Res. Lett.*, *17*, 893-896.
- Sauer, K., E. Dubinin, and K. Baumgartel (1997), Bi-ion structuring in the magnetosheath of Mars - Theoretical modeling, *Adv. Space Res.*, *20*, 137.
- Sauer, K., E. Dubinin, and K. Baumgartel (1998b), Nonlinear MHD waves and discontinuities in the Martian magnetosheath. Observations and 2D bi-ion MHD simulations, *Earth Planets Space*, *50*, 793-801.
- Sauer, K., E. Dubinin, and J. F. McKenzie (2001), New type of soliton in bi-ion plasmas and possible implications, *Geophys. Res. Lett.*, *28*, 3589-3592.
- Sauer, K., E. Dubinin, K. Baumgartel, and V. Tatarov (1998a), Low-frequency electromagnetic waves and instabilities within the Martian bi-ion plasma, *Earth Planets Space*, *50*, 269-278.
- Sauer, K., E. Dubinin, M. Dunlop, K. Baumgartel, and V. Tatarov (1999), Low-frequency electromagnetic waves near and below the proton cyclotron frequency at the AMPTE Ba release: Relevance to comets and Mars, *J. Geophys. Res.*, *104*, 6763-6771.

- Schwartz, S. J., D. Burgess, and J. J. Moses (1996), Low-frequency waves in the Earth's magnetosheath: present status, *Ann. Geophysicae*, *14*, 1134-1150.
- Sergis, N., and X. Moussas (2002), ULF waves at the proton gyrofrequency upstream of the Martian bow shock, based on Mars Global Surveyors measurements, *Solar Phys.*, *209*, 409-419.
- Shinagawa, H. (2000), Our current understanding of the ionosphere of Mars, *Adv. Space Res.*, *26*, 1599-1608.
- Song, P., and C. T. Russell (1999), Time series data analyses in space physics, *Space Sci. Rev.*, *87*, 387-463.
- Sonnerup, B. U. O. and L. J. Cahill Jr. (1967), Magnetopause structure and attitude from Explorer 12 observations, *J. Geophys. Res.*, *72*, 171-183.
- Strangeway, R. J., and G. K. Crawford (1995), VLF waves in the foreshock, *Adv. Space Res.*, *15*, 29-42.
- Tarasov, V., E. Dubinin, S. Perraut, A. Roux, K. Sauer, A. Skalsky, and M. Delva (1998), Wavelet application to the magnetic field turbulence in the upstream region of the Martian bow shock, *Earth Planets Space*, *50*, 699-708.
- Thorne, R. M., and B. T. Tsurutani (1987), Resonant interactions between cometary ions and low frequency electromagnetic waves, *Plan. Space Sci.*, *35*, 1501-1511.

Torrence, C., and G. P. Compo, A Practical Guide to Wavelet Analysis (1998), *Bull. Am. Meteor. Soc.*, 79, 61-78.

Trotignon, J. G., E. Dubinin, R. Grard, S. Barabash, and R. Lundin (1996), Martian planetopause as seen by the plasma wave system onboard Phobos 2, *J. Geophys. Res.*, 101, 24,965-24,977.

Trotignon, J. G., M. Parrot, J. C. Cerisier, M. Menvielle, W. I. Axford, M. Paetzold, R. Warnant, and A. W. Wernik (2000), The plasma environment of Mars: from the shocked solar wind down to the ionosphere, *Planet. Space Sci.*, 48, 1181.

Tsurutani, B. T. (1991a), Cometary plasma waves and instabilities, in *Comets in the Post-Halley Era*, vol. 2, edited by R. L. Newburn et al., pp. 1171-1210, Kluwer Academic, Hingham, Mass.

Tsurutani, B. T. (1991b), Comets: A laboratory for plasma waves and instabilities, in *Cometary Plasma Processes*, *Geophys. Monogr. Ser.*, vol.61, edited by A. D. Johnstone, pp. 189-209, AGU, Washington, D. C.

Tsurutani, B. T. and E. J. Smith (1986a), Hydromagnetic waves and instabilities associated with cometary ion pickup: ICE observations, *Geophys. Res. Lett.*, 13, 263-266.

Tsurutani, B. T. and E. J. Smith (1986b), Strong hydromagnetic turbulence associated with comet Giacobini-Zinner, *Geophys. Res. Lett.*, 13, 259-262.

Vignes, D., C. Mazelle, H. Reme, M. H. Acuña, J. E. P. Connerney, R. P. Lin, D. L. Mitchell, P. A. Cloutier, D. H. Crider, and N. F. Ness (2000), The Solar Wind interaction with Mars: Locations and shapes of the Bow Shock and Magnetic Pile-up Boundary from the observations of the MAG/ER experiment onboard Mars Global Surveyor, *Geophys. Res. Lett.*, *27*, 49-52.

Vozoff, K. (1991), The magnetotelluric method, in *Electromagnetic Methods in Applied Geophysics*, vol. 2, *Application*, edited by M. N. Nabighian, pp. 641-711, Soc. Explor. Geophys., Tulsa, Okla.

Winningham, J. D., R. A. Frahm, J. R. Sharber, A. J. Coates, D. R. Linder, Y. Soobiah, E. Kallio, J. R. Espley, S. Barabash, R. Lundin, and the ASPERA-3 Team (2005), Electron Oscillations in the Martian Sheath, accepted in *Icarus*.

Winske, D. (1986), Origin of large magnetosheath fluctuations in the magnetosheath of Venus, *J. Geophys. Res.*, *91*, 11,951-11,957.